Christie-Blick, N., Austin, J.A., Jr., and Malone, M.J. (Eds.)
Proceedings of the Ocean Drilling Program, Scientific Results Volume 174A

7. Data Report: Bulk Physical Properties of Sediments from ODP Site 1073[1]

Brandon Dugan,[2] David L. Olgaard,[3] Peter B. Flemings,[2] and M.J. Gooch[3]

ABSTRACT

Porosity, permeability, and compressional (*P*-wave) velocity were measured as a function of stress on sediments from Ocean Drilling Program Site 1073, U.S. Mid-Atlantic continental slope. Thin sections, scanning electron microscopy, and X-ray diffraction analyses provided mineralogical characteristics of the samples. Uniaxial strain boundary conditions were imposed on the samples during consolidation tests with the maximum effective axial stress reaching 13 MPa. The maximum effective radial stress necessary to maintain uniaxial strain was 7.6 MPa. Over an effective axial stress interval of 0 to 5.2 MPa, Sample 174A-1073A-26X-2, 82–89 cm (226.65 meters below seafloor [mbsf]), exhibited the largest decrease in porosity (51% to 41%), whereas Sample 71X-1, 2–8 cm (644.70 mbsf), exhibited the smallest decrease in porosity (48% to 45%). All samples showed negligible porosity increases during unloading. The permeability (on the order of 1×10^{-17} m^2) of Sample 174A-1073A-71X-1, 2–8 cm, was twice that measured on Sample 8H-1, 23–26 cm (63.75 mbsf), even though the former was considerably deeper and older. The differences in porosity-stress behavior and permeability between shallow and deep samples is related to lithologic, mineralogic, and diagenetic differences between the sediments above and below the Pliocene–Pleistocene to Miocene unconformity. *P*-wave velocity for Samples 174A-1073A-41X-5, 97–103 cm (372.35 mbsf), and 71X-1, 2–8 cm, increased with decreasing porosity, but did not change significantly during unloading.

[1]Dugan, B., Olgaard, D.L., Flemings, P.B., and Gooch, M.J., 2002. Data report: Bulk physical properties of sediments from ODP Site 1073. *In* Christie-Blick, N., Austin, J.A., Jr., and Malone, M.J. (Eds.), *Proc. ODP, Sci. Results,* 174A, 1–62 [Online]. Available from World Wide Web: <http://www-odp.tamu.edu/publications/174A_SR/VOLUME/CHAPTERS/SR174A07.PDF>. [Cited YYYY-MM-DD]

[2]Department of Geosciences, Penn State University, 320 Deike Building, University Park PA 16802, USA. Correspondence author: **dugan@geosc.psu.edu**
[3]ExxonMobil Upstream Research Company, PO Box 2189, Houston TX 77252-2189, USA.

Initial receipt: 16 July 2002
Acceptance: 24 September 2002
Web publication: 12 December 2002
Ms 174ASR-161

INTRODUCTION

Ocean Drilling Program (ODP) Site 1073 is located on the continental slope off the U.S. Mid-Atlantic coast in 639 m water depth (Fig. F1). The site was drilled to 663 meters below seafloor (mbsf) and penetrated a thick Pleistocene sedimentary package that was underlain by thin layers of Pliocene, Miocene, and Oligocene strata (Fig. F2) (Shipboard Scientific Party, 1998). High core recovery (>97%) allowed for detailed shipboard characterization of lithology, physical properties, and pore fluids. The dominant lithology is undeformed and undercompacted silty clay (Fig. F2). The laboratory data reported here expand the shipboard analyses by constraining the response of physical properties to stress perturbations.

Bulk physical properties, such as porosity and permeability, control strength, deformation, fluid flow, and transport processes in sediments. Stress history, strain path, and lithology influence how these properties evolve and thus affect fluid flow, heat and mass transfer, and slope failure in basins. To evaluate the physical properties of sediments from ODP Site 1073, porosity, permeability, and compressional (*P*-wave) velocity were measured on core samples as a function of stress. Consolidation experiments were performed with uniaxial strain conditions to simulate the conditions that are assumed for the natural burial of sediments in basins. *P*-wave velocity was measured during some of the consolidation experiments. Permeability was measured by constant fluid flux experiments. X-ray diffraction (XRD), scanning electron microscopy (SEM), and thin section analyses provided compositional information on the samples. These analyses link lithologic controls and physical properties. The samples and experiments are summarized in Table T1.

Deformation experiments provide data on the elastic and plastic deformation of sediments. The transition from elastic to dominantly plastic behavior is useful to estimate maximum in situ stress magnitudes (e.g., Casagrande, 1936). Coupled with overburden stress calculations, stress magnitude can be used to evaluate the minimum in situ pore pressure (e.g., Saffer et al., 2000). Deformation behavior also provides insight into how storativity and permeability evolve with burial and compaction. Permeability controls fluid migration and flow paths. The transfer of fluids along permeable strata also influences the stability of sediments (Dugan and Flemings, 2000, 2002). Porosity and effective stress affect sediment shear strength and influence the ability of the slope to resist failure (e.g., Bishop, 1955; Lambe and Whitman, 1979).

F1. Bathymetry near Site 1073, p. 11.

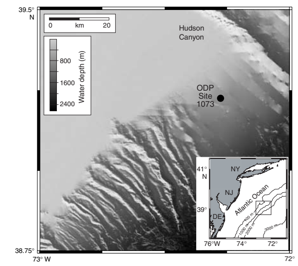

F2. Shipboard observations and interpretations, Site 1073, p. 12.

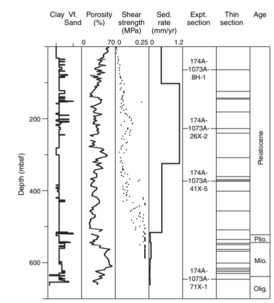

T1. Consolidation, velocity, and permeability samples, p. 19.

EXPERIMENTAL ANALYSIS

Sample Handling and Preparation

Samples were acquired shipboard during ODP Leg 174A. Whole-core samples in the core liner were capped and sealed in wax to maintain natural saturation during refrigerated storage prior to the experiments. For the experiments, each sample was removed from the wax-sealed liner and subsampled with a sharp push corer.

For the experiments, each subsample was trimmed to make a cylinder. Initial cylinder radii were between 1.24 and 1.90 cm, and lengths ranged from 4.88 to 6.69 cm. The mass (m) and volume (V) of each sample was measured, and bulk density was calculated. The sample was then wrapped in filter paper and placed in a neoprene sleeve; porous end caps were placed on the ends of the sample. The porous end caps and filter paper promote drainage of the sample along all surfaces during the experiment.

Initial porosity (ϕ_o) was calculated (Equation 1) using a water density (ρ_w) of 1022 kg/m^3 and the grain density of the sample (ρ_s) (Table T1) (Shipboard Scientific Party, 1998). All variables are defined in the nomenclature table (Table T2). This calculation assumes 100% water saturation. The pore water used in the experiments had a density and composition that matched the average in situ pore water at ODP Site 1073. The dimensions, mass, and the initial porosity were measured for each sample before they were placed in the deformation chamber.

$$\phi_o = (\rho_s - m/V)/(\rho_s - \rho_w). \quad (1)$$

Consolidation Tests

Consolidation experiments were performed on five silty clay samples from four depths (Table T1; Fig. F2). Volume change was measured as a function of effective stress. These experiments yielded porosity-stress relations (Tables T3, T4, T5, T6, T7; Fig. F3) and estimates of the earth pressure at rest (Equation 2), which relates the effective horizontal stress (σ_h) to the effective vertical stress (σ_v) (Figs. F4, F5) (Lambe and Whitman, 1979):

$$K_o = \sigma_h/\sigma_v. \quad (2)$$

The first stage of the experiment was isostatic pressurizing to ~0.2 MPa. Axial and radial strains were monitored throughout this loading phase to calculate pore volume changes. Deformation then continued with uniaxial strain boundary conditions (zero radial strain) at a constant loading rate of 0.7 kPa/min. Uniaxial strain loading continued up to an effective axial stress of 5.2 MPa. Unloading (decreasing effective stress) was performed at a constant unloading rate of 0.7 kPa/min to an axial stress of 4.2 MPa. Sample 174A-1073A-8H-1, 17–22 cm, was unloaded to 4.2 MPa and then reloaded to 13 MPa at a load rate of 0.7 kPa/min. All other samples were rapidly unloaded from 4.2 MPa to ambient pressure. Axial stress was controlled during all stages of loading and unloading. During the uniaxial strain portion of the test, effective radial stress was dynamically controlled to maintain zero radial strain.

Assuming that the solid grains are incompressible and that fully drained conditions are maintained, the measured volumes (V) were related to porosity (ϕ) (Equation 3) (Tables T3, T4, T5, T6, T7; Fig. F3). Nomenclature and units are defined in Table T2.

$$\phi_{\sigma+\Delta\sigma} = [V_{\sigma}\phi_{\sigma} + (V_{\sigma+\Delta\sigma} - V_{\sigma})]/V_{\sigma+\Delta\sigma}. \quad (3)$$

Axial and radial drainage of pore fluids combined with a slow loading rate facilitated fluid expulsion to ensure fully drained conditions. Pore pressure and fluid expulsion measurements verified that drained conditions were achieved at least during the loading portion of the experiments.

T2. Nomenclature, p. 20.

T3. Stress and porosity (174A-1073A-8H-1, 17–22 cm), p. 21.

T4. Stress and porosity (174A-1073A-26X-2, 76–82 cm), p. 22.

T5. Stress and porosity (174A-1073A-26X-2, 82–89cm), p. 23.

T6. Stress and porosity (174A-1073A-41X-5, 97–103 cm), p. 24.

T7. Stress and porosity (174A-1073A-71X-1, 2–8 cm), p. 25.

F3. Deformation behavior for Site 1073 samples, p. 13.

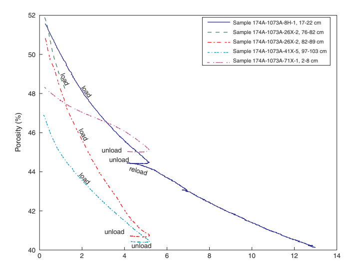

F4. Earth pressure at rest during deformation experiments, p. 14.

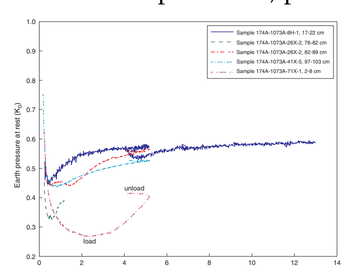

Velocity Measurements

Compressional (*P*-wave) velocity (V_P) was measured during the consolidation experiments on Samples 174A-1073A-41X-5, 97–103 cm, and 71X-1, 2–8 cm (Table T8; Fig. F6). Sonic traveltimes (Δt) were measured immediately after a stress increment. Velocities were calculated from the net travel time through the sample (Δt – Δt_{caps}) and the instantaneous sample length (l) (Equation 4) (nomenclature and units are defined in Table T2):

$$V_P = l/(\Delta t - \Delta t_{caps}). \quad (4)$$

Permeability Measurements

Permeability (k) was measured on Samples 174A-1073A-8H-1, 23–26 cm, and 71X-1, 9–14 cm (Table T9; Figs. F7, F8). These samples were taken adjacent to Samples 174A-1073A-8H-1, 17–22 cm, and 71X-1, 2–8 cm, which were used in the consolidation experiments. Permeability was measured at a variety of stresses by applying a constant differential pressure (ΔP) across the sample and monitoring the fluid flux (Q) until it reached steady state (Equation 5):

$$k = \mu Q l / \pi r^2 \Delta P. \quad (5)$$

A brine pore fluid (6% potassium chloride) with a dynamic viscosity (μ) of 9.7×10^{-4} Pa·s was used. All tests were run at a constant temperature of 22.2°C. Nomenclature and units are defined in Table T2.

Sample Characterization

XRD, SEM, and thin section analyses were used to evaluate the mineralogy, fabric, and grain morphology of all samples (Tables T10, T11; "Appendix," p. 7). The high silt and clay content of the samples precluded mineral identification in thin section but allowed qualitative inspection of grain size and porosity distributions. XRD analyses provided mineralogical characterizations (Table T10). SEM analyses of Samples 174A-1073A-8H-1, 17–22 cm, and 71X-1, 2–8 cm, provided a breakdown of clay content and more quantitative mineralogical characterization (Tables T10, T11). Weight percents were calculated using a proprietary ExxonMobil mineral identification system that is based on chemically based point counts and the X-ray spectrum of the samples.

RESULTS

The Pleistocene samples (Samples 174A-1073A-8H-1, 7–22 cm; 26X-2, 76–82 cm; 26X-2, 82–89 cm; and 41X-5, 97–103 cm) initially exhibited rapid porosity decrease with increasing effective stress, followed by a decreased rate of porosity loss (Fig. F3). In contrast, the Oligocene Sample 174A-1073A-71X-1, 2–8 cm, showed a slow porosity decrease followed by a more rapid decrease. Over the effective stress interval 0–5.2 MPa, the overall porosity loss in this Oligocene sample was significantly less than that for the Pleistocene samples.

Compaction behavior varied with mineralogy and lithology. Sample 174A-1073A-26X-2, 82–89 cm, showed the largest porosity decrease during unloading from 0 to 5.2 MPa (51%–41%), whereas Sample 71X-

F5. K_o from 0 to 6 MPa effective axial stress, p. 15.

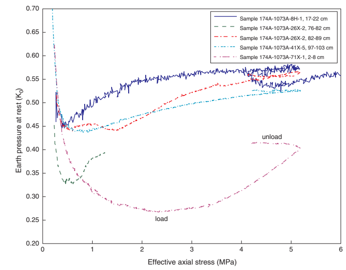

T8. Velocity and porosity, p. 26.

F6. *P*-wave velocity vs. porosity, p. 16.

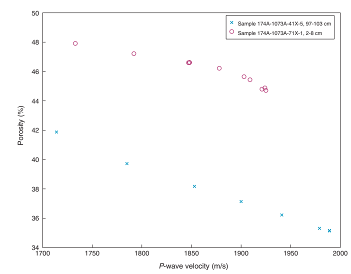

T9. Stress and permeability, p. 27.

F7. Permeability at different states of stress, p. 17.

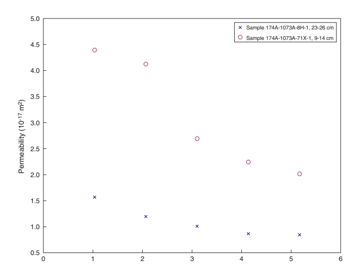

F8. Permeability-porosity relations, p. 18.

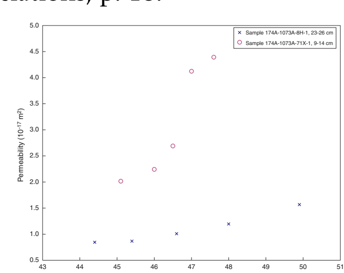

1, 2–8 cm, showed the smallest decrease (48%–45%) (Fig. F3). Sample 174A-1073A-26X-2, 82–89 cm, had no calcite and moderate clay content (Table T10; "Appendix," p. 7), whereas Sample 71X-1, 2–8 cm, had lower clay content (Tables T10, T11; "Appendix," p. 7). Samples 174A-1073A-8H-1, 17–22 cm, 26X-2, 76–82 cm, and 41X-5, 97–103 cm, had similar deformation characteristics and similar compositions (Table T10; "Appendix," p. 7). Sample 174A-1073A-71X-1, 2–8 cm, had different deformation behavior and a different composition, most notably a significant fraction of glauconite grains (Table T11; "Appendix," p. 7).

T10. XRD, p. 28.

T11. SEM, p. 29.

The earth pressure at rest (K_o) for each experiment began at 1 because the initial loading was isostatic. After sample equilibration and the emplacement of uniaxial strain boundary conditions, all samples exhibited a decrease in K_o followed by an increase (Figs. F4, F5). An unload–reload cycle on Sample 174A-1073A-8H-1, 17–22 cm, shows a local K_o minimum at 4.79 MPa effective axial stress, which is near the maximum previous effective stress established in the laboratory (5.15 MPa) (Figs. F4, F5). Sample 174A-1073A-71X-1, 2–8 cm, exhibits a different K_o stress behavior, which likely reflects the different lithology, mineralogy, and cementation of this sample relative to the Pleistocene samples.

P-wave velocity was similar for Samples 174A-1073A-41X-5, 97–103 cm, and 71X-1, 2–8 cm, even though the samples had different porosities (Fig. F6). Each sample showed a subtle velocity increase with decreasing porosity. Sample 174A-1073A-41X-5, 97–103 cm, had a nearly linear increase in velocity over the porosity decrease from 42% to 35%. The similarity in velocity between the samples, even though the porosities are significantly different, is believed to be caused by intergranular cement in Sample 174A-1073A-71X-1, 2–8 cm.

Permeability of Samples 174A-1073A-8H-1, 23–26 cm, and 71X-1, 9–14 cm, decreased with increasing effective stress and decreasing porosity (Figs. F7, F8). Sample 174A-1073A-8H-1, 23–26 cm, has a gradual and minor decrease in permeability. Sample 174A-1073A-71X-1, 9–14 cm, shows an abrupt permeability decrease between 2 and 3 MPa, which is coincident with the stress range over which porosity in the adjacent sample (Sample 174A-1073A-71X-1, 2–8 cm) begins to decrease more rapidly and at the stress where K_o is at a minimum (Figs. F3, F5, F7). The permeability of Sample 174A-1073A-8H-1, 23–26 cm, is lower than Sample 71X-1, 9–14 cm, as a result of the higher clay content of the shallower sample (Fig. F8; Tables T10, T11).

ACKNOWLEDGMENTS

ExxonMobil Upstream Research Company provided laboratory facilities, research time, and technical expertise for this project. Permeability measurements were made by Core Laboratories in Houston, TX. This research used samples and/or data provided by the Ocean Drilling Program (ODP). ODP is sponsored by the U.S. National Science Foundation (NSF) and participating countries under management of Joint Oceanographic Institutions (JOI), Inc. This research was supported by NSF Grant EAR-0003467 (Flemings), the Penn State GeoFluids Consortium (Amerada Hess, Anadarko Petroleum, BHP, Burlington Resources, ChevronTexaco, Conoco, Devon Energy, ExxonMobil, Pan Canadian, Phillips Petroleum, Shell Oil, and Unocal), and ExxonMobil Upstream Research Company.

REFERENCES

Bishop, A.W., 1955. The use of the slip circle in the stability of earth slopes. *Geotechnique,* 5:7–17.

Blum, P., 1994. *Index Properties: ODP Shipboard Laboratory Manual,* Version 155, College Station, TX (Ocean Drilling Program).

Casagrande, A., 1936. The determination of pre-consolidation load and its practical significance. *In* Casagrande, A., Rutledge, P.C., and Watson, J.D. (Eds.)*, Proc. 1st Int. Conf. Soil Mech. Found. Eng.,* Am. Soc. Civ. Eng., 3:60–64.

Dugan, B., and Flemings, P.B., 2000. Overpressure and fluid flow in the New Jersey Continental Slope: implications for slope failure and cold seeps. *Science,* 289:288–291.

————, 2002. Fluid flow and stability of the US Continental Slope offshore New Jersey from the Pleistocene to the present. *Geofluids,* 2:137–146.

Lambe, T.W., and Whitman, R.V., 1979. *Soil Mechanics* (SI ver.): New York (Wiley).

Saffer, D.M., Silver, E.A., Fisher, A.T., Tobin, H., and Moran, K., 2000. Inferred pore pressures at the Costa Rica subduction zone: implications for dewatering processes. *Earth Planet. Sci. Lett.,* 177:193–207.

Shipboard Scientific Party, 1998. Site 1073. *In* Austin, J.A., Jr., Christie-Blick, N., Malone, M.J., et al., *Proc. ODP, Init. Repts.,* 174A: College Station, TX (Ocean Drilling Program), 153–191.

APPENDIX

Figures AF1, AF2, AF3, AF4, AF5, AF6, AF7, AF8, AF9, and AF10 are thin section images of shipboard physical properties samples that show the variations in lithology, grain size, and porosity for Site 1073. All thin sections were prepared with a clear epoxy. Samples are located in Figure F2.

Figures AF11, AF12, AF13, AF14, AF15, and AF16 are thin section images from whole-core samples that were used in the experimental study. A blue epoxy was used in sample preparation. Samples are located in Figure F2.

Figures AF17, AF18, AF19, AF20, AF21, AF22, AF23, AF24, AF25, AF26, AF27, AF28, AF29, AF30, AF31, AF32, and AF33 are SEM images from Samples 174A-1073A-8H-1, 17–22 cm, and 71X-1, 2–8 cm. Image locations are identified on Figures AF11 and AF16.

AF1. Thin sections (174A-1073A-14H-2, 99–101 cm, and 16H-4, 101–103 cm), p. 30.

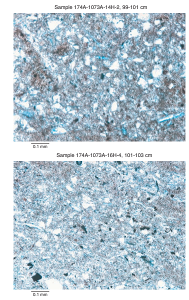

AF2. Thin sections (174A-1073A-20H-2, 143–145 cm, and 27X-4, 117–119 cm), p. 31.

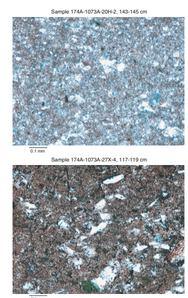

AF3. Thin sections (174A-1073A-34X-6, 26–28 cm, and 41X-2, 50–52 cm), p. 32.

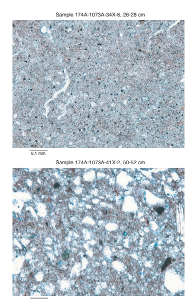

AF4. Thin sections (174A-1073A-41X-5, 50–52 cm, and 44X-5, 13–15 cm), p. 33.

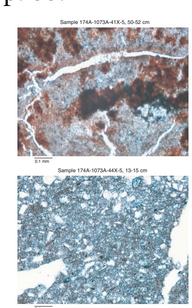

AF5. Thin sections (174A-1073A-50X-5, 86–88 cm, and 56X-2, 97–99 cm), p. 34.

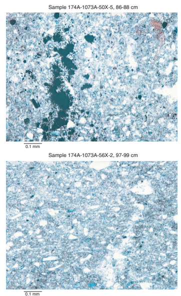

AF6. Thin sections (174A-1073A-59X-1, 62–64 cm, and 60X-3, 43–45 cm), p. 35.

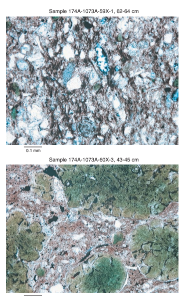

AF7. Thin sections (174A-1073A-60X-6, 47–49 cm, and 62X-2, 110–112 cm), p. 36.

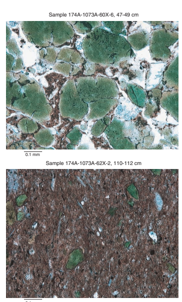

AF8. Thin sections (174A-1073A-62X-5, 122–124 cm, and 66X-2, 130–132 cm), p. 37.

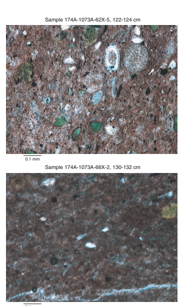

AF9. Thin sections (174A-1073A-67X-5, 124–126 cm, and 68X-2, 118–120 cm), p. 38.

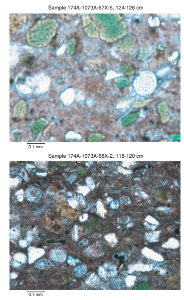

AF10. Thin sections (174A-1073A-68X-5, 113–115 cm, and 69X-2, 133–135 cm), p. 39.

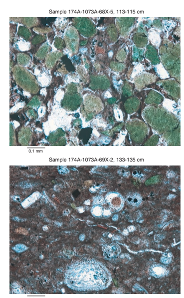

AF11. Thin section (174A-1073A-8H-1, 17–22 cm), p. 40.

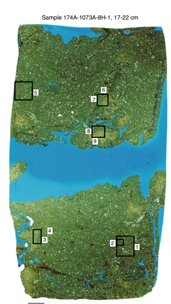

AF12. Thin section (174A-1073A-41X-5, 97–103 cm), p. 41.

AF13. Thin section (174A-1073A-26X-2, 76–82 cm), p. 42.

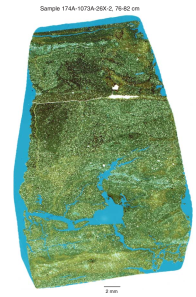

AF14. Thin section (174A-1073A-41X-5, 97–103 cm), p. 43.

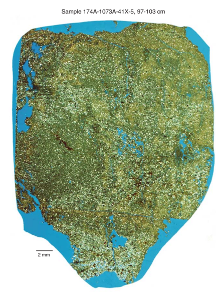

AF15. Thin section (174A-1073A-51X-1, 22–37 cm), p. 44.

AF16. Thin section (174A-1073A-71X-1, 2–8 cm), p. 45.

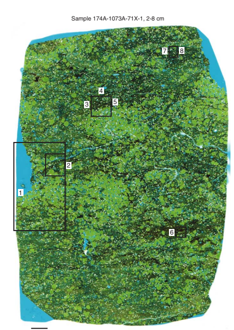

AF17. SEM image at 72×, p. 46.

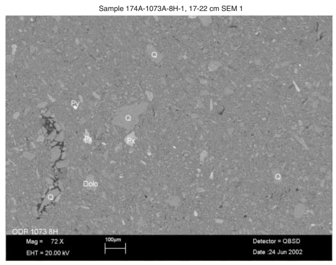

AF18. SEM image at 400×, p. 47.

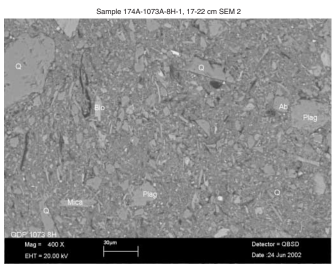

AF19. SEM image at 62×, p. 48.

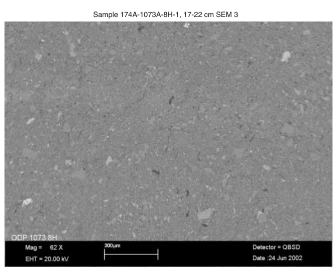

AF20. SEM image at 1130×, p. 49.

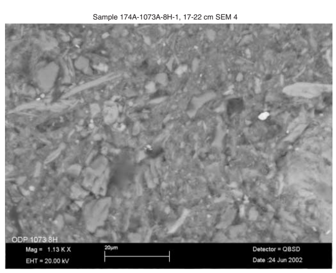

AF21. SEM image at 60×, p. 50.

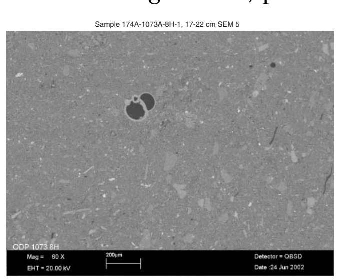

AF22. SEM image at 63×, p. 51.

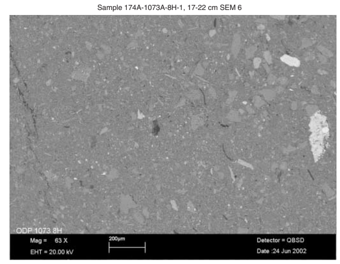

AF23. SEM image at 450×, p. 52.

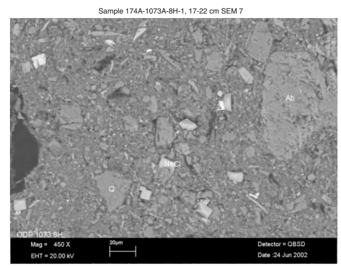

AF24. SEM image at 72×, p. 53.

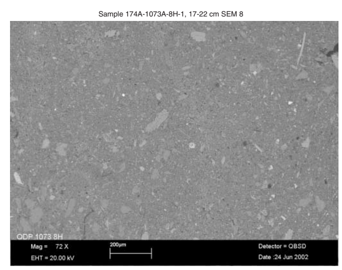

AF25. SEM image at 600×, p. 54.

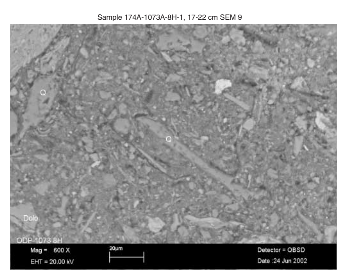

AF26. SEM image at 15×, p. 55.

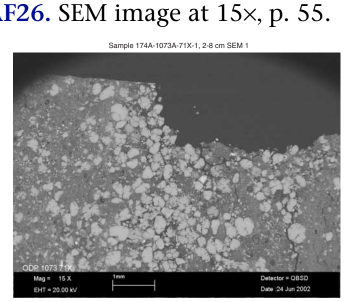

AF27. SEM image at 60×, p. 56.

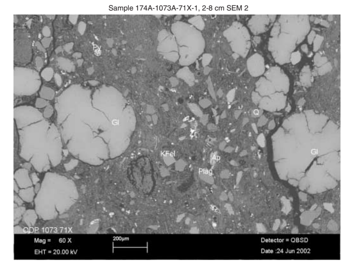

AF28. SEM image at 15×, p. 57.

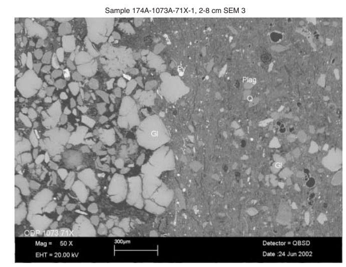

AF29. SEM image at 300×, p. 58.

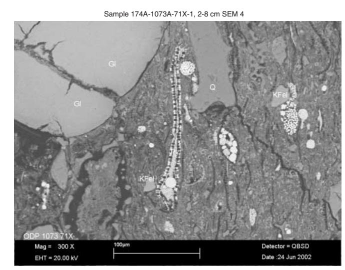

AF30. SEM image at 335×, p. 59.

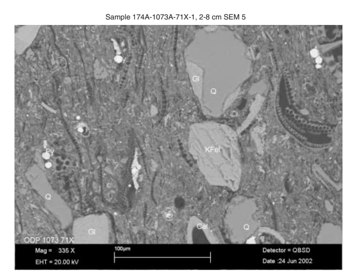

AF31. SEM image at 1000×, p. 60.

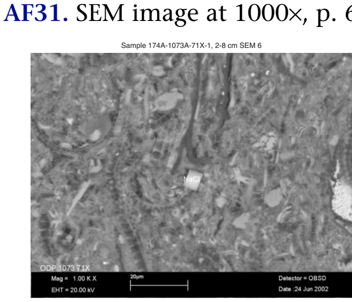

AF32. SEM image at 1000×, p. 61.

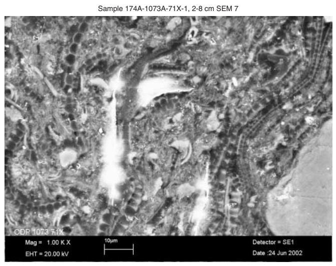

AF33. SEM image at 1000×, p. 62.

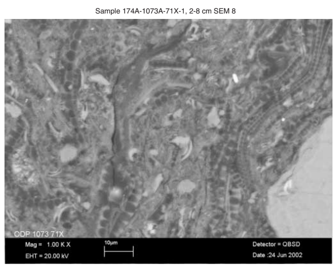

Figure F1. Bathymetry in the region of ODP Site 1073. Inset map shows the location of the study region relative to the U.S. east coast.

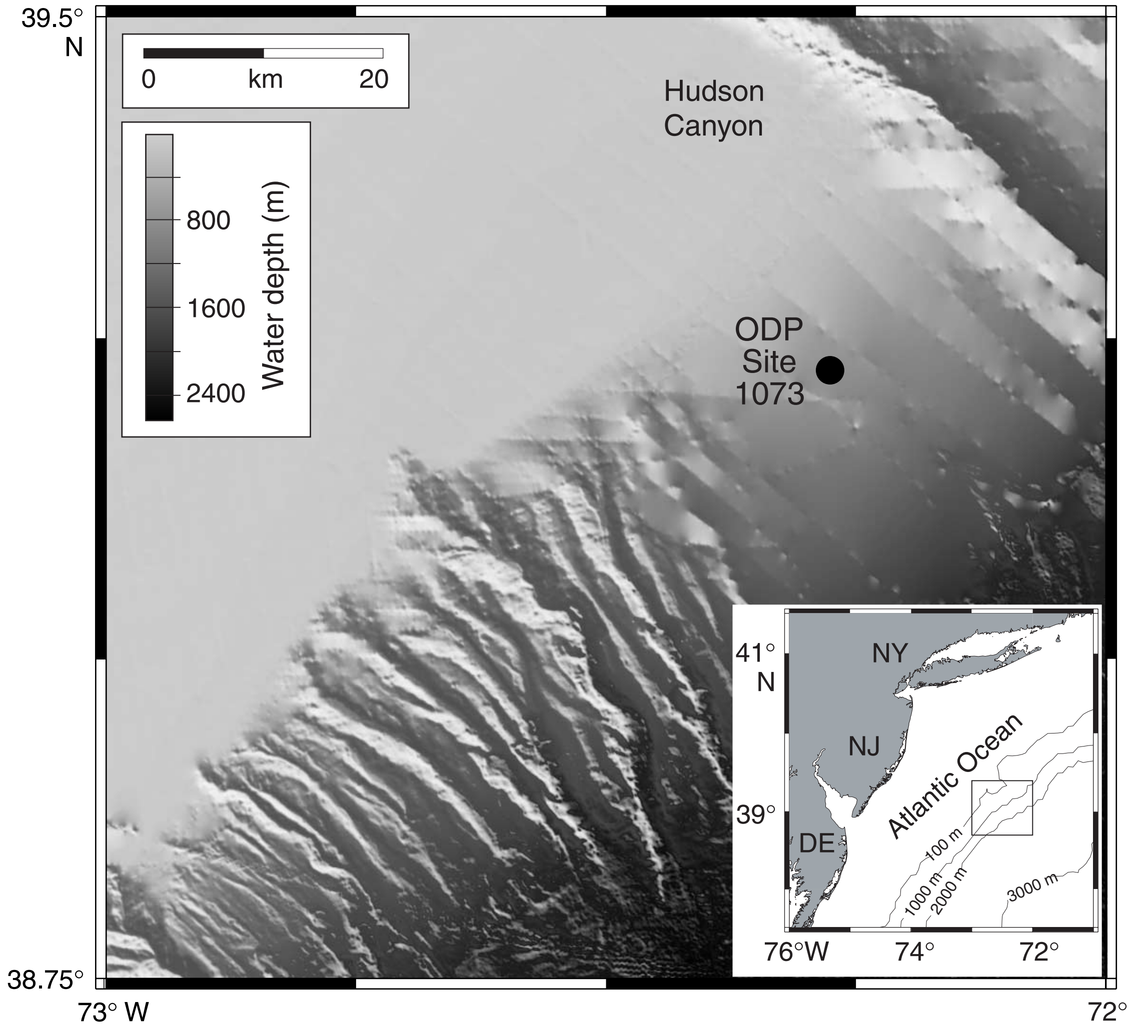

Figure F2. Shipboard observations and interpretations from ODP Site 1073 (Shipboard Scientific Party, 1998). Lithology is dominated by silty clay. Porosity was determined shipboard by wet and dry mass and volume measurements of core samples (Blum, 1994; Shipboard Scientific Party, 1998). Shear strength measurements are a combination of automated shear strength and penetrometer measurements. Sedimentation rates are based on shipboard-derived ages. Expt. Section = the location of samples that were used in this experimental study. Thin section = the depths for which thin sections were made for grain size, lithologic, and mineralogic interpretation. Thin section and SEM images are provided in the "Appendix," p. 7.

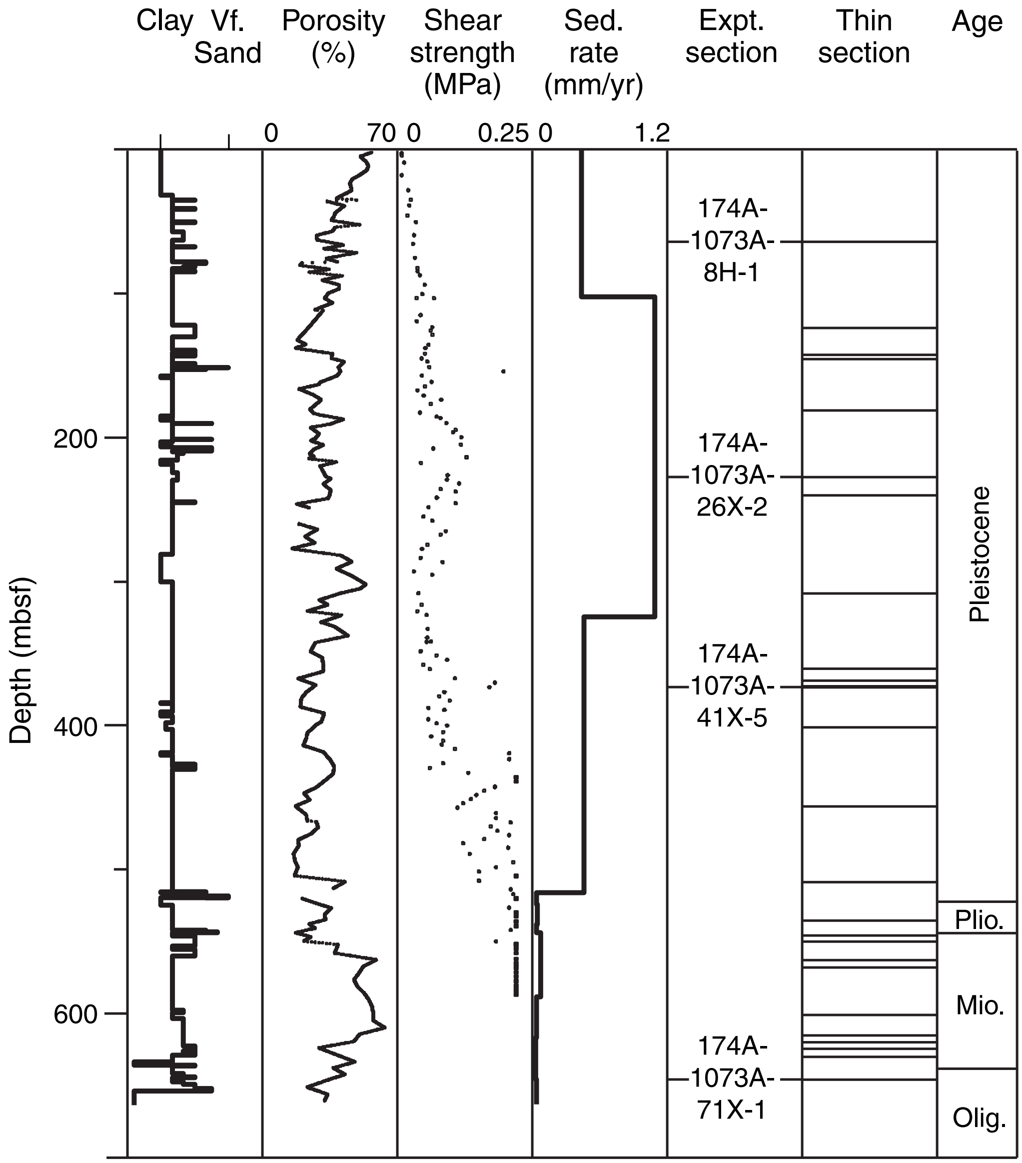

Figure F3. Deformation (porosity-stress) behavior for samples from ODP Site 1073. Sample locations are identified in Figure F2, p. 12. Raw data are provided in Tables T3, p. 21, T4, p. 22, T5, p. 23, T6, p. 24, and T7, p. 25.

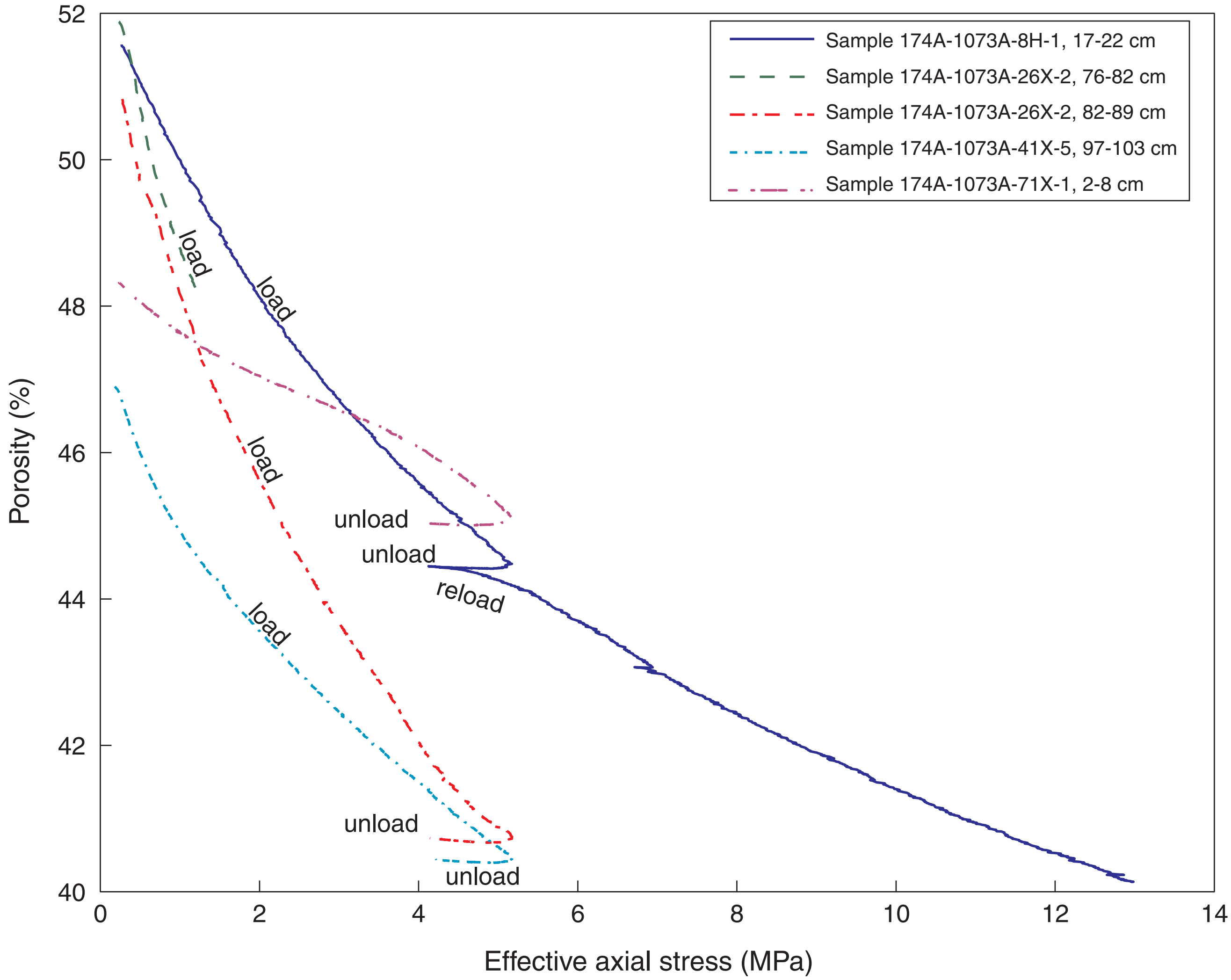

Figure F4. Earth pressure at rest (K_o) for samples during deformation experiments. An example of the load/unload path is labeled for Sample 174A-1073A-71X-1, 2–8 cm. All samples exhibit an initial decrease in K_o followed by an increase. Samples 174A-1073A-8H-1, 17–22 cm, 26X-2, 82–89 cm, and 41X-5, 97–103 cm, approach approximately the same K_o value. Lower K_o for Sample 174A-1073A-71X-1, 2–8 cm, reflects its difference in lithology from the other samples. Raw data are provided in Tables T3, p. 21, T4, p. 22, T5, p. 23, T6, p. 24, and T7, p. 25.

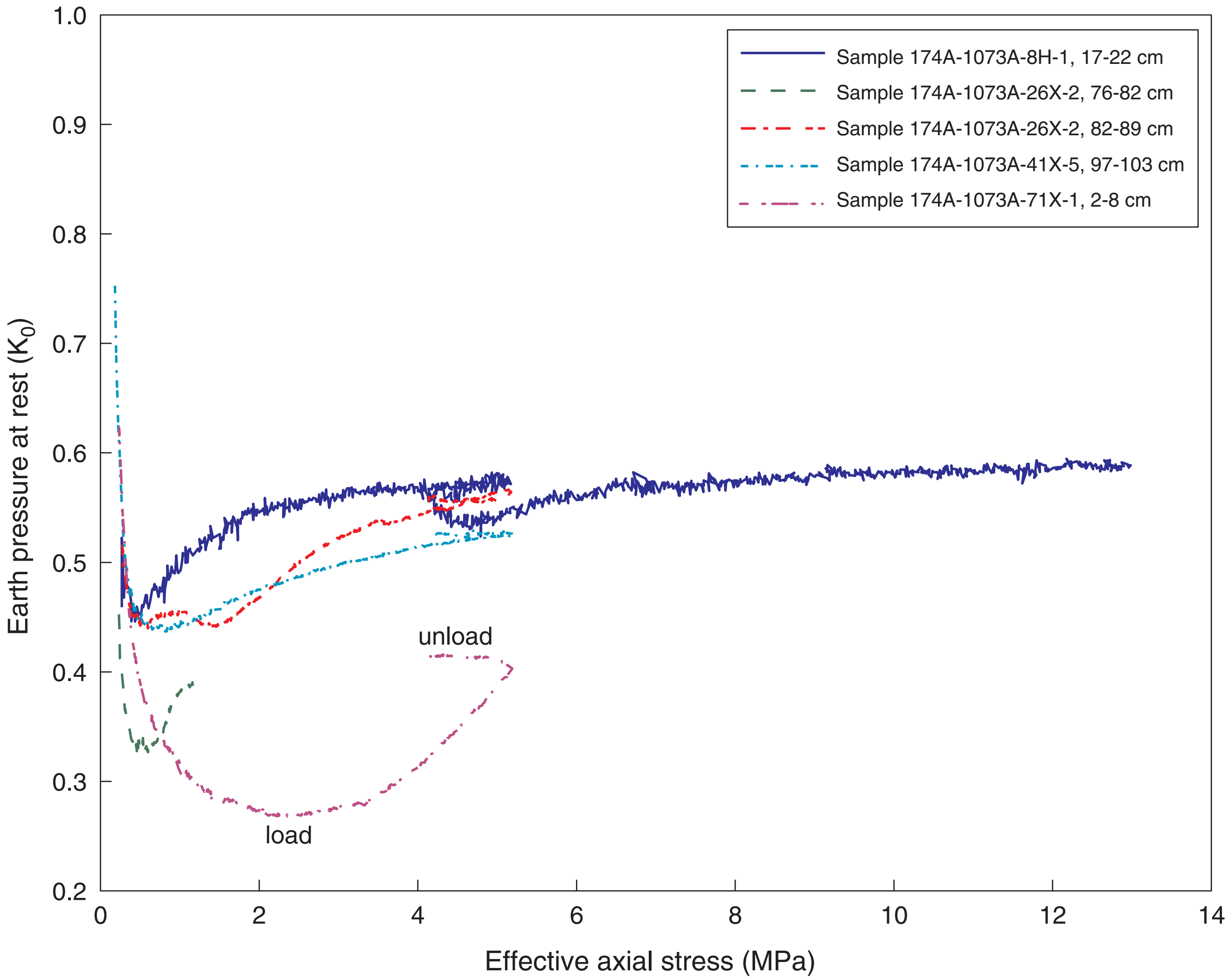

Figure F5. Enlarged view (0- to 6-MPa effective axial stress) of the K_o data presented in Figure **F4**, p. 14, to emphasize the variation in K_o during initial loading. Raw data are provided in Tables **T3**, p. 21, **T4**, p. 22, **T5**, p. 23, **T6**, p. 24, and **T7**, p. 25.

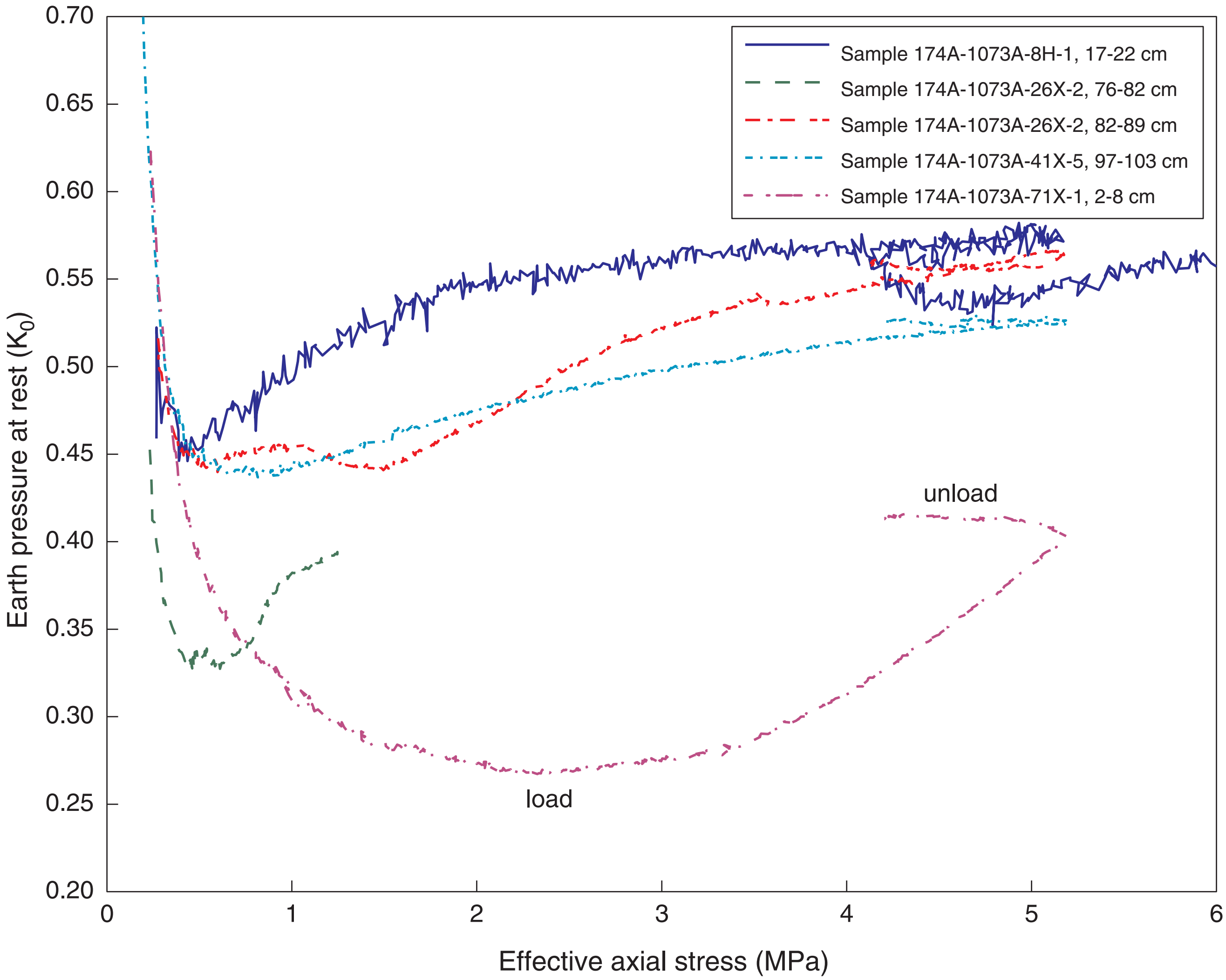

Figure F6. *P*-wave velocity as a function of porosity for Samples 174A-1073A-41X-5, 97–103 cm, and 71X-1, 2–8 cm, measured during uniaxial strain experiments. The samples have similar velocity but Sample 71X-1, 2–8 cm, has higher porosity. This behavior is interpreted to reflect partial cementation of grains in Sample 71X-1, 2–8 cm. Data are provided in Table **T8**, p. 26.

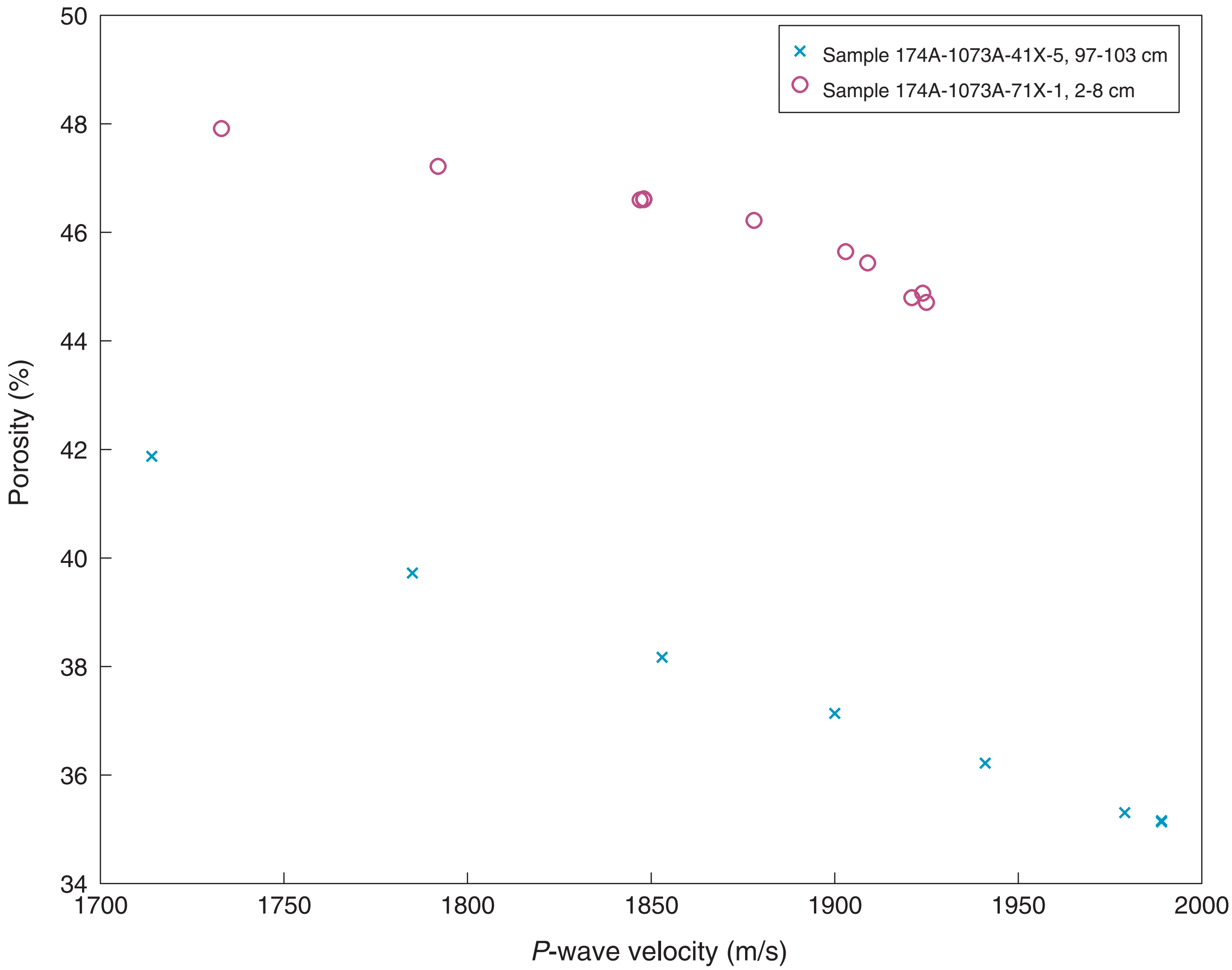

Figure F7. Measured permeability at different states of stress for Samples 174A-1073A-8H-1, 23–26 cm, and 71X-1, 9–14 cm. These samples were taken adjacent to Samples 174A-1073A-8H-1, 17–22 cm, and 71X-1, 2–8 cm, which were used in the deformation experiments. Step decrease in permeability of Sample 174A-1073A-71X-1, 9–14 cm, between 2 and 3 MPa effective stress reflects change in stress-strain behavior of the sample as shown in K_o variation (Fig. **F5**, p. 15). Data are provided in Table **T9**, p. 27.

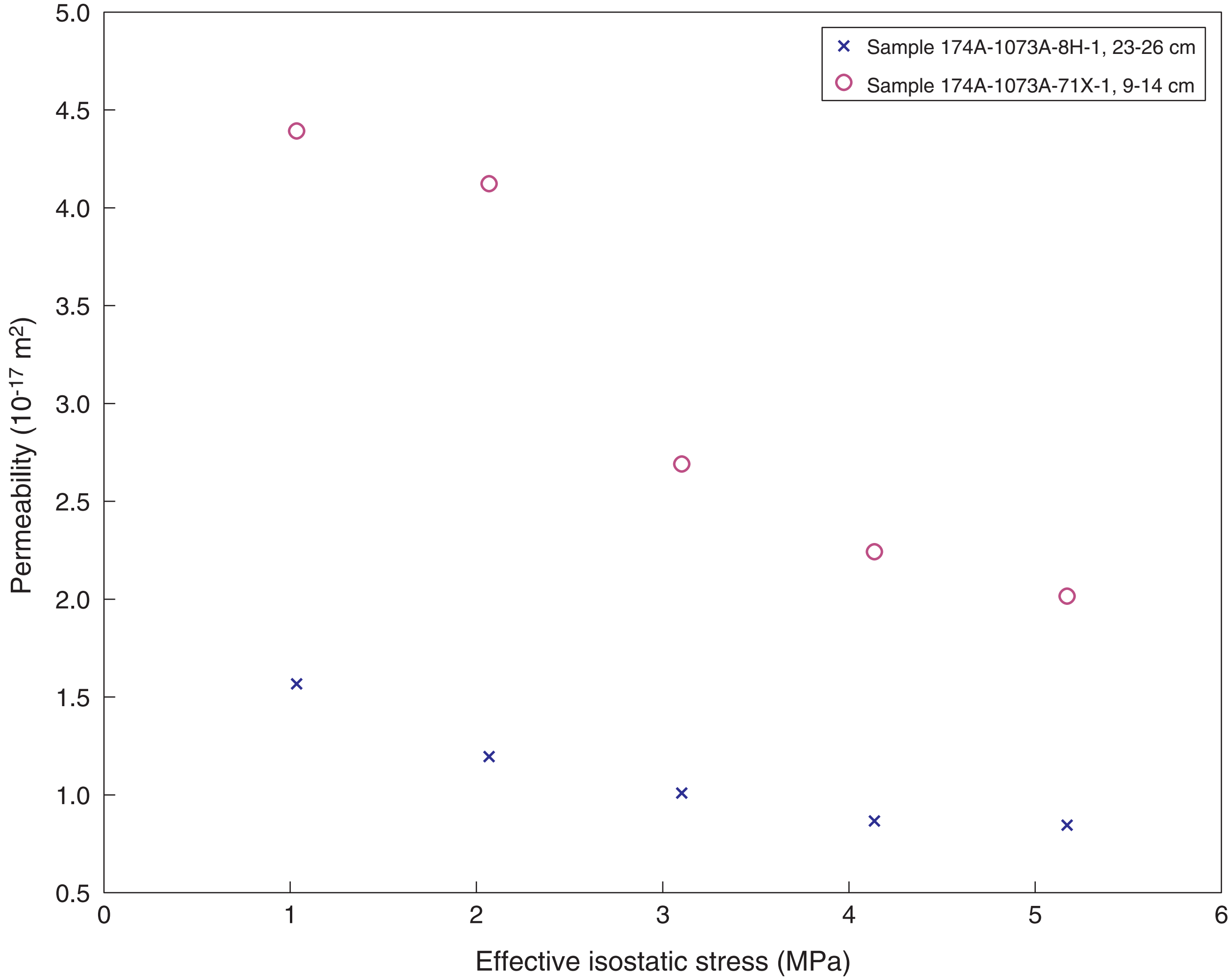

Figure F8. Permeability of Samples 174A-1073A-8H-1, 23–26 cm, and 71X-1, 9–14 cm, referenced to porosity. Porosity is approximated based on the stress state of the permeability experiment and the porosity calculations on Samples 174A-1073A-8H-1, 17–22 cm, and 71X-1, 2–8 cm. Data are provided in Table T9, p. 27.

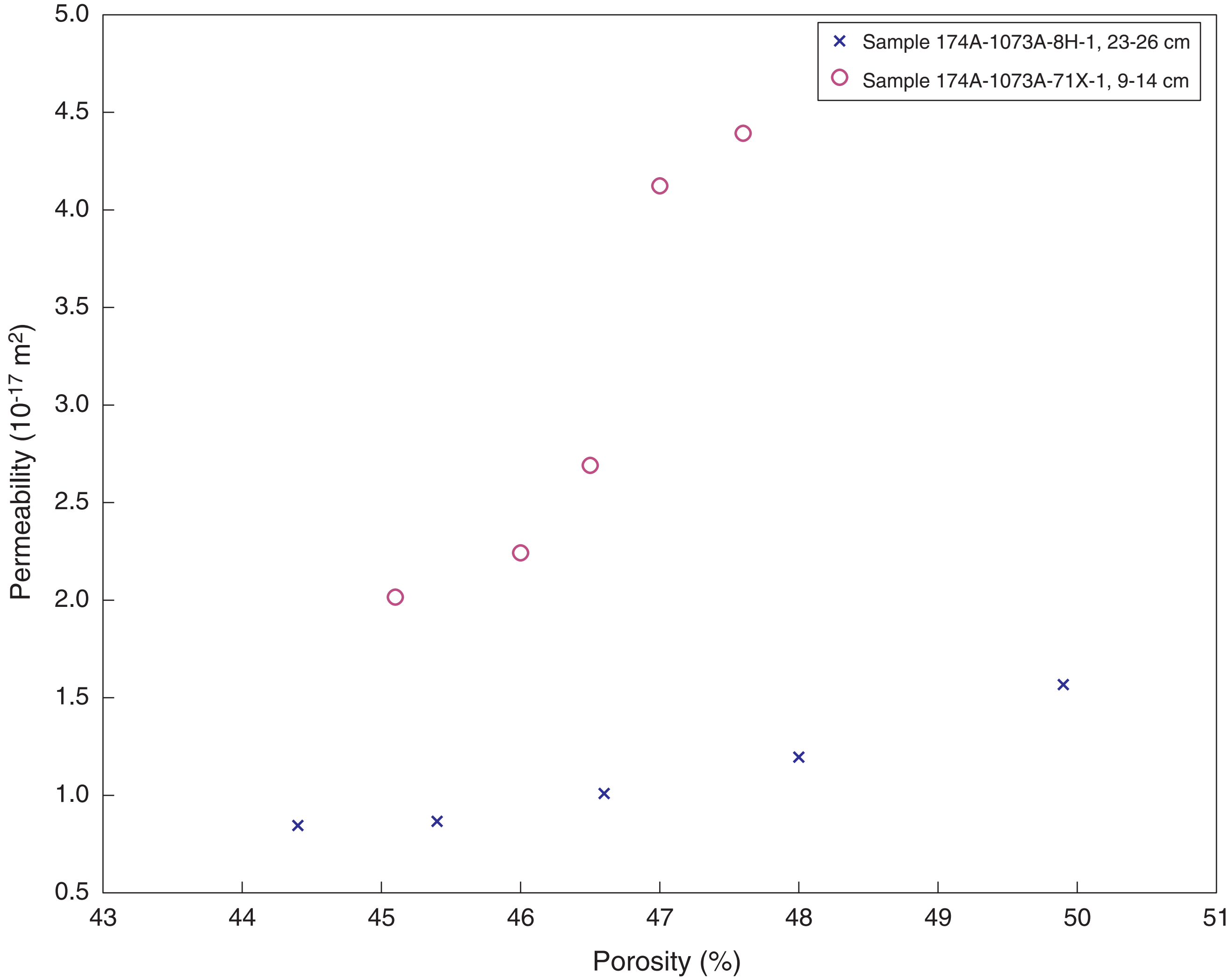

Table T1. Samples used in consolidation, velocity, and permeability experiments.

Core, section, interval (cm)	Age	Depth (mbsf)	Grain density (kg/m^3)	Experiment	Characterization
174A-1073A-					
8H-1, 17-22	Pleistocene	63.75	2720	Consolidation	XRD, thin section, SEM
8H-1, 23-26	Pleistocene	63.75	2720	Permeability	
16H-3, 135-150	Pleistocene	143.95			XRD, thin section
26X-2, 76-82	Pleistocene	226.65	2740	Consolidation	XRD, thin section
26X-2, 82-89	Pleistocene	226.65	2740	Consolidation	
41X-5, 97-103	Pleistocene	372.35	2740	Consolidation, velocity	XRD, thin section
51X-1, 22-37	Pleistocene	459.52			XRD, thin section
58X-6, 15-30	Pliocene	532.45			XRD
71X-1, 2-8	late Oligocene	644.70	2650	Consolidation, velocity	XRD, thin section, SEM
71X-1, 9-14	late Oligocene	644.70	2650	Permeability	

Notes: XRD = X-ray diffraction. SEM = scanning electron microscopy.

Table T2. Nomenclature.

Variable	Definition	Dimensions	SI units
k	Permeability	L^2	m^2
K_o	Earth pressure at rest	Dimensionless	—
l	Sample length	L	m
m	Sample mass	M	kg
Q	Fluid flux	L^3/T	m^3/s
r	Sample radius	L	m
V	Sample volume	L^3	m^3
V_P	*P*-wave velocity	L/T	m/s
ΔP	Pressure differential	M/LT^2	Pa
Δt	Total traveltime	T	s
Δt_{caps}	Traveltime through end caps	T	s
ϕ	Porosity	Dimensionless	—
ρ_s	Grain density	M/L^3	kg/m^3
ρ_w	Fluid density	M/L^3	kg/m^3
μ	Dynamic viscosity	M/LT	Pa•s
σ	Effective stress	M/LT^2	Pa
$\Delta\sigma$	Effective stress increment	M/LT^2	Pa
σ_h	Effective horizontal (radial) stress	M/LT^2	Pa
σ_v	Effective vertical (axial) stress	M/LT^2	Pa

Table T3. Stress and porosity measurements from Sample 174A-1073A-8H-1, 17–22 cm.

Effective axial stress (Mpa)	Effective radial stress (Mpa)	Length (cm)	Radius (cm)	Volume (cm^3)	Porosity (%)	Boundary condition
0.000	0.000	4.876	1.251	23.953	52.007	Isostatic
0.125	0.058	4.876	1.251	23.953	52.006	Isostatic
0.191	0.095	4.859	1.251	23.869	51.838	Isostatic
0.226	0.092	4.846	1.250	23.806	51.710	Isostatic
0.263	0.129	4.836	1.251	23.756	51.609	Isostatic
0.274	0.142	4.834	1.251	23.748	51.592	Isostatic
0.257	0.123	4.834	1.251	23.748	51.593	Isostatic
0.265	0.134	4.834	1.251	23.747	51.590	Isostatic
0.252	0.121	4.834	1.251	23.749	51.594	Isostatic
0.270	0.137	4.833	1.251	23.744	51.583	Isostatic
0.254	0.121	4.833	1.251	23.743	51.582	Isostatic
0.260	0.129	4.833	1.251	23.744	51.585	Isostatic
0.241	0.140	4.835	1.251	23.755	51.606	Isostatic
0.244	0.137	4.835	1.251	23.755	51.605	Isostatic
0.237	0.116	4.835	1.251	23.752	51.601	Isostatic
0.268	0.123	4.832	1.251	23.739	51.574	Uniaxial strain
0.269	0.131	4.830	1.251	23.730	51.555	Uniaxial strain
0.268	0.140	4.830	1.251	23.730	51.555	Uniaxial strain
0.295	0.138	4.828	1.251	23.718	51.531	Uniaxial strain
0.301	0.143	4.825	1.251	23.706	51.506	Uniaxial strain
0.319	0.154	4.822	1.251	23.687	51.467	Uniaxial strain
0.339	0.162	4.818	1.251	23.669	51.431	Uniaxial strain
0.366	0.174	4.813	1.251	23.645	51.381	Uniaxial strain
0.386	0.179	4.807	1.251	23.617	51.322	Uniaxial strain
0.390	0.174	4.805	1.251	23.605	51.299	Uniaxial strain
0.403	0.184	4.802	1.251	23.592	51.272	Uniaxial strain
0.417	0.188	4.799	1.251	23.578	51.243	Uniaxial strain
0.428	0.196	4.797	1.251	23.564	51.214	Uniaxial strain
0.435	0.194	4.794	1.251	23.551	51.187	Uniaxial strain
0.457	0.210	4.791	1.251	23.537	51.157	Uniaxial strain
0.481	0.218	4.786	1.251	23.512	51.106	Uniaxial strain
0.493	0.223	4.782	1.251	23.493	51.066	Uniaxial strain
0.517	0.235	4.779	1.251	23.476	51.032	Uniaxial strain
0.518	0.236	4.776	1.251	23.465	51.009	Uniaxial strain
0.525	0.242	4.775	1.251	23.458	50.994	Uniaxial strain
0.538	0.247	4.773	1.251	23.449	50.974	Uniaxial strain
0.551	0.255	4.770	1.251	23.433	50.941	Uniaxial strain
0.572	0.269	4.766	1.251	23.416	50.906	Uniaxial strain
0.585	0.275	4.764	1.251	23.404	50.881	Uniaxial strain
0.588	0.272	4.762	1.251	23.393	50.857	Uniaxial strain
0.597	0.276	4.759	1.251	23.381	50.833	Uniaxial strain
0.607	0.278	4.757	1.251	23.371	50.810	Uniaxial strain
0.626	0.291	4.754	1.251	23.356	50.779	Uniaxial strain
0.652	0.310	4.751	1.251	23.341	50.749	Uniaxial strain
0.670	0.319	4.748	1.251	23.324	50.713	Uniaxial strain
0.681	0.327	4.745	1.251	23.309	50.680	Uniaxial strain
0.680	0.323	4.742	1.251	23.297	50.654	Uniaxial strain
0.689	0.330	4.740	1.251	23.288	50.636	Uniaxial strain
0.706	0.337	4.738	1.251	23.276	50.611	Uniaxial strain
0.732	0.343	4.734	1.251	23.257	50.569	Uniaxial strain
0.750	0.357	4.730	1.251	23.236	50.526	Uniaxial strain
0.746	0.356	4.727	1.251	23.222	50.495	Uniaxial strain
0.771	0.365	4.724	1.251	23.207	50.463	Uniaxial strain
0.796	0.387	4.720	1.251	23.190	50.427	Uniaxial strain
0.805	0.373	4.718	1.251	23.178	50.400	Uniaxial strain
0.814	0.395	4.715	1.251	23.164	50.371	Uniaxial strain
0.803	0.378	4.713	1.251	23.155	50.352	Uniaxial strain
0.843	0.412	4.710	1.251	23.138	50.316	Uniaxial strain
0.845	0.420	4.707	1.251	23.126	50.290	Uniaxial strain
0.859	0.416	4.705	1.251	23.115	50.267	Uniaxial strain
0.880	0.429	4.702	1.251	23.100	50.234	Uniaxial strain
0.897	0.445	4.699	1.251	23.085	50.201	Uniaxial strain
0.913	0.448	4.697	1.251	23.073	50.176	Uniaxial strain
0.923	0.454	4.694	1.251	23.061	50.150	Uniaxial strain

Note: Only a portion of this table appears here. The complete table is available in **ASCII format.**

Table T4. Stress and porosity measurements from Sample 174A-1073A-26X-2, 76–82 cm.

Effective axial stress (MPa)	Effective radial stress	Length (cm)	Radius (cm)	Volume (cm^3)	Porosity (%)	Boundary Condition
0.000	0.000	5.842	1.241	28.256	52.400	Isostatic
0.112	0.048	5.841	1.241	28.256	52.367	Isostatic
0.184	0.093	5.814	1.243	28.230	52.323	Isostatic
0.201	0.078	5.797	1.242	28.106	52.113	Isostatic
0.171	0.043	5.774	1.233	27.573	51.187	Isostatic
0.239	0.112	5.744	1.242	27.833	51.644	Isostatic
0.235	0.107	5.744	1.242	27.833	51.643	Isostatic
0.243	0.114	5.739	1.243	27.850	51.674	Isostatic
0.242	0.115	5.739	1.243	27.868	51.704	Isostatic
0.249	0.121	5.735	1.244	27.877	51.719	Isostatic
0.229	0.101	5.736	1.244	27.894	51.750	Isostatic
0.244	0.116	5.733	1.245	27.898	51.757	Isostatic
0.249	0.122	5.734	1.245	27.907	51.772	Isostatic
0.233	0.106	5.735	1.245	27.917	51.790	Isostatic
0.256	0.130	5.732	1.245	27.919	51.793	Isostatic
0.248	0.120	5.733	1.245	27.929	51.810	Isostatic
0.253	0.127	5.731	1.246	27.935	51.819	Isostatic
0.251	0.125	5.732	1.246	27.940	51.828	Isostatic
0.236	0.108	5.733	1.246	27.948	51.843	Isostatic
0.252	0.125	5.731	1.246	27.953	51.851	Isostatic
0.242	0.116	5.733	1.246	27.962	51.867	Isostatic
0.254	0.126	5.731	1.246	27.965	51.871	Isostatic
0.233	0.105	5.734	1.246	27.974	51.887	Isostatic
0.232	0.105	5.734	1.246	27.974	51.887	Uniaxial strain
0.240	0.105	5.733	1.246	27.970	51.880	Uniaxial strain
0.244	0.103	5.732	1.246	27.965	51.871	Uniaxial strain
0.245	0.101	5.731	1.246	27.960	51.864	Uniaxial strain
0.258	0.106	5.729	1.246	27.952	51.849	Uniaxial strain
0.268	0.107	5.726	1.246	27.937	51.824	Uniaxial strain
0.277	0.109	5.723	1.246	27.921	51.797	Uniaxial strain
0.288	0.111	5.718	1.246	27.899	51.757	Uniaxial strain
0.293	0.112	5.717	1.246	27.890	51.743	Uniaxial strain
0.297	0.111	5.713	1.246	27.872	51.712	Uniaxial strain
0.307	0.112	5.709	1.246	27.853	51.678	Uniaxial strain
0.311	0.114	5.707	1.246	27.845	51.665	Uniaxial strain
0.333	0.119	5.700	1.246	27.808	51.600	Uniaxial strain
0.353	0.124	5.689	1.246	27.757	51.511	Uniaxial strain
0.369	0.128	5.681	1.246	27.714	51.437	Uniaxial strain
0.381	0.130	5.673	1.246	27.678	51.374	Uniaxial strain
0.391	0.132	5.667	1.246	27.649	51.323	Uniaxial strain
0.404	0.136	5.661	1.246	27.620	51.271	Uniaxial strain
0.412	0.138	5.656	1.246	27.593	51.223	Uniaxial strain
0.422	0.140	5.650	1.246	27.563	51.170	Uniaxial strain
0.437	0.147	5.643	1.246	27.531	51.114	Uniaxial strain
0.443	0.148	5.637	1.246	27.504	51.064	Uniaxial strain
0.444	0.148	5.634	1.246	27.486	51.034	Uniaxial strain
0.449	0.149	5.630	1.246	27.469	51.004	Uniaxial strain
0.451	0.150	5.627	1.246	27.455	50.978	Uniaxial strain
0.453	0.150	5.625	1.246	27.443	50.957	Uniaxial strain
0.456	0.151	5.623	1.246	27.431	50.935	Uniaxial strain
0.461	0.151	5.620	1.246	27.418	50.911	Uniaxial strain
0.449	0.150	5.618	1.246	27.411	50.899	Uniaxial strain
0.451	0.150	5.618	1.246	27.409	50.895	Uniaxial strain
0.451	0.149	5.617	1.246	27.405	50.889	Uniaxial strain
0.467	0.156	5.615	1.246	27.395	50.871	Uniaxial strain
0.468	0.154	5.614	1.246	27.387	50.857	Uniaxial strain
0.472	0.157	5.611	1.246	27.376	50.837	Uniaxial strain
0.474	0.157	5.609	1.246	27.366	50.819	Uniaxial strain
0.475	0.157	5.607	1.246	27.356	50.801	Uniaxial strain
0.475	0.160	5.606	1.246	27.350	50.790	Uniaxial strain
0.486	0.164	5.603	1.246	27.336	50.765	Uniaxial strain
0.494	0.163	5.599	1.246	27.318	50.731	Uniaxial strain
0.502	0.167	5.596	1.246	27.300	50.699	Uniaxial strain
0.515	0.172	5.590	1.246	27.273	50.651	Uniaxial strain

Note: Only a portion of this table appears here. The complete table is available in ASCII format.

Table T5. Stress and porosity measurements from Sample 174A-1073A-26X-2, 82–89 cm.

Effective axial stress (MPa)	Effective radial stress (MPa)	Length (cm)	Radius (cm)	Volume (cm^3)	Porosity (%)	Boundary Condition
0.000	0.000	6.694	1.253	33.042	51.784	Isostatic
0.097	0.042	6.694	1.253	33.042	51.784	Isostatic
0.218	0.134	6.527	1.261	32.614	51.151	Isostatic
0.298	0.182	6.487	1.263	32.498	50.977	Isostatic
0.250	0.128	6.489	1.263	32.497	50.975	Isostatic
0.241	0.121	6.488	1.263	32.491	50.965	Isostatic
0.243	0.123	6.488	1.263	32.492	50.968	Isostatic
0.250	0.128	6.486	1.263	32.486	50.958	Isostatic
0.239	0.119	6.487	1.263	32.488	50.961	Isostatic
0.251	0.131	6.484	1.263	32.479	50.948	Isostatic
0.252	0.130	6.484	1.263	32.478	50.946	Isostatic
0.252	0.131	6.483	1.263	32.473	50.939	Isostatic
0.235	0.115	6.484	1.263	32.474	50.940	Isostatic
0.238	0.119	6.483	1.263	32.470	50.935	Isostatic
0.244	0.124	6.482	1.263	32.468	50.931	Isostatic
0.253	0.133	6.479	1.263	32.459	50.917	Isostatic
0.244	0.123	6.480	1.263	32.460	50.920	Isostatic
0.239	0.118	6.480	1.263	32.458	50.916	Isostatic
0.231	0.110	6.480	1.263	32.456	50.913	Isostatic
0.230	0.110	6.479	1.263	32.454	50.909	Isostatic
0.243	0.122	6.478	1.263	32.449	50.902	Isostatic
0.229	0.109	6.478	1.263	32.448	50.901	Isostatic
0.250	0.129	6.475	1.263	32.439	50.888	Isostatic
0.264	0.143	6.472	1.263	32.430	50.874	Isostatic
0.274	0.143	6.469	1.263	32.417	50.854	Isostatic
0.277	0.143	6.466	1.263	32.402	50.831	Uniaxial strain
0.283	0.144	6.463	1.263	32.382	50.801	Uniaxial strain
0.284	0.145	6.460	1.263	32.367	50.778	Uniaxial strain
0.279	0.141	6.459	1.263	32.364	50.774	Uniaxial strain
0.283	0.141	6.458	1.263	32.358	50.764	Uniaxial strain
0.294	0.146	6.453	1.263	32.336	50.731	Uniaxial strain
0.305	0.149	6.449	1.263	32.313	50.696	Uniaxial strain
0.313	0.152	6.443	1.263	32.283	50.649	Uniaxial strain
0.326	0.156	6.437	1.263	32.252	50.603	Uniaxial strain
0.328	0.157	6.432	1.263	32.227	50.565	Uniaxial strain
0.335	0.158	6.427	1.263	32.203	50.527	Uniaxial strain
0.345	0.163	6.422	1.263	32.178	50.490	Uniaxial strain
0.352	0.164	6.417	1.263	32.156	50.455	Uniaxial strain
0.358	0.166	6.412	1.263	32.130	50.415	Uniaxial strain
0.367	0.169	6.407	1.263	32.107	50.379	Uniaxial strain
0.375	0.172	6.402	1.263	32.079	50.336	Uniaxial strain
0.380	0.175	6.398	1.263	32.059	50.306	Uniaxial strain
0.383	0.175	6.394	1.263	32.040	50.276	Uniaxial strain
0.384	0.175	6.391	1.263	32.025	50.252	Uniaxial strain
0.385	0.175	6.388	1.263	32.010	50.229	Uniaxial strain
0.397	0.179	6.384	1.263	31.990	50.199	Uniaxial strain
0.406	0.184	6.380	1.263	31.969	50.165	Uniaxial strain
0.414	0.186	6.376	1.263	31.948	50.132	Uniaxial strain
0.415	0.189	6.373	1.263	31.932	50.108	Uniaxial strain
0.419	0.189	6.369	1.263	31.915	50.080	Uniaxial strain
0.434	0.196	6.365	1.263	31.892	50.045	Uniaxial strain
0.445	0.200	6.359	1.263	31.863	49.999	Uniaxial strain
0.455	0.205	6.352	1.263	31.830	49.948	Uniaxial strain
0.466	0.211	6.346	1.263	31.799	49.898	Uniaxial strain
0.473	0.213	6.341	1.263	31.773	49.857	Uniaxial strain
0.481	0.216	6.337	1.263	31.754	49.827	Uniaxial strain
0.493	0.220	6.333	1.263	31.731	49.792	Uniaxial strain
0.492	0.218	6.330	1.263	31.718	49.770	Uniaxial strain
0.490	0.218	6.329	1.263	31.711	49.760	Uniaxial strain
0.485	0.216	6.328	1.263	31.707	49.754	Uniaxial strain
0.491	0.218	6.326	1.263	31.698	49.739	Uniaxial strain
0.492	0.219	6.325	1.263	31.694	49.733	Uniaxial strain
0.492	0.220	6.324	1.263	31.690	49.727	Uniaxial strain
0.493	0.220	6.324	1.263	31.688	49.723	Uniaxial strain

Note: Only a portion of this table appears here. The complete table is available in ASCII format.

Table T6. Stress and porosity measurements from Sample 174A-1073A-41X-5, 97–103 cm.

Effective Axial Stress (Mpa)	Effective Radial Stress (Mpa)	Length (cm)	Radius (cm)	Volume (cm^3)	Porosity (%)	Boundary Condition
0.000	0.000	5.880	1.900	66.697	46.916	Isostatic
0.076	0.057	5.880	1.900	66.697	46.916	Isostatic
0.150	0.117	5.848	1.904	66.607	46.844	Isostatic
0.236	0.189	5.820	1.909	66.620	46.855	Isostatic
0.183	0.137	5.822	1.909	66.664	46.890	Isostatic
0.195	0.148	5.821	1.909	66.658	46.886	Isostatic
0.195	0.148	5.822	1.909	66.662	46.889	Isostatic
0.188	0.141	5.822	1.909	66.666	46.892	Isostatic
0.185	0.138	5.822	1.909	66.668	46.893	Isostatic
0.188	0.141	5.821	1.909	66.666	46.892	Isostatic
0.188	0.142	5.821	1.909	66.664	46.890	Isostatic
0.181	0.133	5.822	1.909	66.672	46.896	Isostatic
0.187	0.141	5.821	1.909	66.664	46.890	Isostatic
0.181	0.137	5.822	1.909	66.675	46.899	Isostatic
0.167	0.131	5.823	1.909	66.691	46.911	Isostatic
0.182	0.137	5.822	1.909	66.678	46.901	Uniaxial strain
0.202	0.137	5.820	1.909	66.647	46.876	Uniaxial strain
0.216	0.139	5.818	1.909	66.625	46.859	Uniaxial strain
0.225	0.140	5.816	1.909	66.604	46.842	Uniaxial strain
0.244	0.146	5.812	1.909	66.562	46.809	Uniaxial strain
0.247	0.144	5.809	1.909	66.526	46.780	Uniaxial strain
0.260	0.147	5.806	1.909	66.486	46.748	Uniaxial strain
0.266	0.148	5.802	1.909	66.450	46.719	Uniaxial strain
0.274	0.150	5.800	1.909	66.423	46.697	Uniaxial strain
0.276	0.149	5.798	1.909	66.396	46.676	Uniaxial strain
0.284	0.151	5.796	1.909	66.374	46.658	Uniaxial strain
0.286	0.151	5.794	1.909	66.353	46.641	Uniaxial strain
0.293	0.152	5.792	1.909	66.333	46.625	Uniaxial strain
0.303	0.156	5.789	1.909	66.295	46.595	Uniaxial strain
0.314	0.157	5.785	1.909	66.252	46.560	Uniaxial strain
0.323	0.160	5.782	1.909	66.212	46.528	Uniaxial strain
0.334	0.165	5.778	1.909	66.173	46.496	Uniaxial strain
0.342	0.166	5.774	1.909	66.129	46.461	Uniaxial strain
0.357	0.172	5.771	1.909	66.085	46.425	Uniaxial strain
0.365	0.172	5.766	1.909	66.034	46.383	Uniaxial strain
0.385	0.183	5.762	1.909	65.987	46.345	Uniaxial strain
0.394	0.184	5.758	1.909	65.942	46.308	Uniaxial strain
0.392	0.185	5.755	1.909	65.911	46.283	Uniaxial strain
0.412	0.192	5.752	1.909	65.877	46.255	Uniaxial strain
0.418	0.190	5.749	1.909	65.838	46.224	Uniaxial strain
0.430	0.197	5.746	1.909	65.799	46.192	Uniaxial strain
0.441	0.202	5.742	1.909	65.760	46.160	Uniaxial strain
0.458	0.207	5.739	1.909	65.720	46.127	Uniaxial strain
0.464	0.208	5.735	1.909	65.678	46.093	Uniaxial strain
0.483	0.218	5.731	1.909	65.631	46.054	Uniaxial strain
0.495	0.222	5.726	1.909	65.580	46.012	Uniaxial strain
0.503	0.225	5.723	1.909	65.540	45.980	Uniaxial strain
0.521	0.236	5.720	1.909	65.506	45.951	Uniaxial strain
0.526	0.235	5.717	1.909	65.477	45.927	Uniaxial strain
0.539	0.240	5.714	1.909	65.439	45.896	Uniaxial strain
0.557	0.247	5.710	1.909	65.392	45.857	Uniaxial strain
0.571	0.256	5.706	1.909	65.347	45.820	Uniaxial strain
0.588	0.262	5.702	1.909	65.301	45.781	Uniaxial strain
0.601	0.265	5.698	1.909	65.254	45.742	Uniaxial strain
0.614	0.272	5.695	1.909	65.215	45.710	Uniaxial strain
0.628	0.278	5.691	1.909	65.178	45.679	Uniaxial strain
0.638	0.282	5.689	1.909	65.146	45.652	Uniaxial strain
0.652	0.286	5.685	1.909	65.106	45.619	Uniaxial strain
0.666	0.293	5.682	1.909	65.068	45.587	Uniaxial strain
0.685	0.301	5.678	1.909	65.028	45.554	Uniaxial strain
0.694	0.306	5.675	1.909	64.989	45.521	Uniaxial strain
0.712	0.314	5.672	1.909	64.952	45.491	Uniaxial strain
0.725	0.319	5.668	1.909	64.916	45.460	Uniaxial strain
0.734	0.323	5.666	1.909	64.886	45.435	Uniaxial strain

Note: Only a portion of this table appears here. The complete table is available in **ASCII format.**

Table T7. Stress and porosity measurements from Sample 174A-1073A-71X-1, 2–8 cm.

Effective Axial Stress (MPa)	Effective Radial Stress (MPa)	Length (cm)	Radius (cm)	Volume (cm^3)	Porosity (%)	Boundary Condition
0.000	0.000	5.740	1.868	62.897	48.514	Isostatic
0.049	0.024	5.740	1.868	62.897	48.514	Isostatic
0.218	0.180	5.715	1.870	62.751	48.394	Isostatic
0.309	0.257	5.706	1.870	62.680	48.337	Isostatic
0.185	0.132	5.714	1.869	62.716	48.366	Isostatic
0.170	0.116	5.715	1.869	62.723	48.372	Isostatic
0.180	0.127	5.714	1.869	62.718	48.367	Isostatic
0.201	0.147	5.713	1.869	62.713	48.363	Isostatic
0.177	0.123	5.714	1.869	62.719	48.368	Isostatic
0.168	0.114	5.715	1.869	62.722	48.371	Isostatic
0.204	0.151	5.713	1.869	62.711	48.362	Isostatic
0.171	0.118	5.714	1.869	62.721	48.370	Isostatic
0.198	0.145	5.713	1.869	62.713	48.363	Isostatic
0.190	0.137	5.713	1.869	62.715	48.365	Isostatic
0.176	0.123	5.714	1.869	62.720	48.369	Isostatic
0.182	0.129	5.714	1.869	62.720	48.369	Isostatic
0.180	0.127	5.714	1.869	62.719	48.369	Isostatic
0.198	0.144	5.713	1.869	62.713	48.363	Isostatic
0.239	0.147	5.708	1.869	62.662	48.321	Uniaxial strain
0.236	0.147	5.708	1.869	62.661	48.320	Uniaxial strain
0.265	0.152	5.706	1.869	62.631	48.296	Uniaxial strain
0.279	0.152	5.703	1.869	62.607	48.276	Uniaxial strain
0.300	0.157	5.701	1.869	62.581	48.254	Uniaxial strain
0.318	0.158	5.699	1.869	62.555	48.233	Uniaxial strain
0.332	0.161	5.697	1.869	62.540	48.221	Uniaxial strain
0.335	0.161	5.696	1.869	62.528	48.210	Uniaxial strain
0.359	0.164	5.694	1.869	62.506	48.193	Uniaxial strain
0.367	0.165	5.693	1.869	62.493	48.181	Uniaxial strain
0.366	0.167	5.692	1.869	62.485	48.175	Uniaxial strain
0.382	0.169	5.691	1.869	62.470	48.162	Uniaxial strain
0.387	0.168	5.690	1.869	62.463	48.156	Uniaxial strain
0.387	0.168	5.690	1.869	62.456	48.151	Uniaxial strain
0.423	0.178	5.687	1.869	62.430	48.129	Uniaxial strain
0.433	0.179	5.686	1.869	62.416	48.118	Uniaxial strain
0.445	0.184	5.685	1.869	62.407	48.110	Uniaxial strain
0.443	0.181	5.684	1.869	62.397	48.102	Uniaxial strain
0.449	0.184	5.684	1.869	62.391	48.097	Uniaxial strain
0.470	0.187	5.682	1.869	62.375	48.084	Uniaxial strain
0.488	0.191	5.680	1.869	62.356	48.067	Uniaxial strain
0.495	0.195	5.680	1.869	62.346	48.060	Uniaxial strain
0.490	0.194	5.679	1.869	62.343	48.057	Uniaxial strain
0.493	0.194	5.679	1.869	62.339	48.054	Uniaxial strain
0.491	0.193	5.679	1.869	62.338	48.053	Uniaxial strain
0.521	0.200	5.677	1.869	62.322	48.040	Uniaxial strain
0.544	0.205	5.676	1.869	62.302	48.023	Uniaxial strain
0.557	0.207	5.674	1.869	62.280	48.005	Uniaxial strain
0.571	0.214	5.673	1.869	62.269	47.995	Uniaxial strain
0.576	0.214	5.672	1.869	62.261	47.989	Uniaxial strain
0.575	0.214	5.672	1.869	62.258	47.986	Uniaxial strain
0.586	0.217	5.671	1.869	62.249	47.978	Uniaxial strain
0.591	0.218	5.670	1.869	62.242	47.973	Uniaxial strain
0.594	0.217	5.669	1.869	62.234	47.966	Uniaxial strain
0.616	0.222	5.668	1.869	62.223	47.957	Uniaxial strain
0.630	0.226	5.667	1.869	62.210	47.946	Uniaxial strain
0.644	0.232	5.666	1.869	62.200	47.938	Uniaxial strain
0.642	0.228	5.665	1.869	62.190	47.929	Uniaxial strain
0.654	0.235	5.665	1.869	62.182	47.923	Uniaxial strain
0.647	0.231	5.664	1.869	62.178	47.919	Uniaxial strain
0.664	0.235	5.664	1.869	62.169	47.912	Uniaxial strain
0.670	0.237	5.663	1.869	62.162	47.906	Uniaxial strain
0.674	0.236	5.662	1.869	62.155	47.900	Uniaxial strain
0.694	0.240	5.661	1.869	62.143	47.890	Uniaxial strain
0.689	0.241	5.661	1.869	62.137	47.884	Uniaxial strain
0.715	0.246	5.659	1.869	62.122	47.872	Uniaxial strain

Note: Only a portion of this table appears here. The complete table is available in ASCII format.

Table T8. Velocity-porosity measurements, Site 1073.

Core, section, interval (cm)	Effective axial stress (MPa)	Porosity (%)	*P*-wave velocity (m/s)
174A-1073A-41X-5, 97–103			
	0.185	41.872	1714
	1.042	39.723	1785
	2.181	38.169	1853
	3.094	37.136	1900
	4.023	36.221	1941
	5.015	35.307	1979
	5.176	35.158	1989
	4.222	35.135	1989
174A-1073A-71X-1, 2–8			
	0.180	47.912	1733
	0.987	47.218	1792
	2.050	46.617	1848
	2.053	46.604	1848
	2.058	46.599	1847
	2.940	46.220	1878
	4.107	45.646	1903
	4.403	45.435	1909
	5.098	44.880	1924
	5.170	44.798	1921
	4.303	44.711	1925

Table T9. Stress and permeability measurements, Site 1073.

Core, section, interval (cm)	Isostatic effective stress (MPa)	Length (cm)	Radius (cm)	Fluid flux (cm^3/s)	Differential Pressure (MPa)	Permeability (m^2)	Approximate Porosity (%)
174A-1073A-8H-1, 23–26							
	1.034	2.430	1.215	8.600E–05	0.278	1.567E–17	49.9
	2.068	2.400	1.200	7.567E–05	0.325	1.195E–17	48.0
	3.103	2.380	1.185	6.317E–05	0.325	1.009E–17	46.6
	4.137	2.370	1.175	5.467E–05	0.332	8.660E–18	45.4
	5.171	2.340	1.175	5.383E–05	0.332	8.447E–18	44.4
174A-1073A-71X-1, 9–14							
	1.034	5.000	1.890	1.600E–04	0.157	4.393E–17	47.6
	2.068	4.980	1.885	2.883E–04	0.302	4.123E–17	47.0
	3.103	4.960	1.885	1.917E–04	0.307	2.691E–17	46.5
	4.137	4.950	1.880	1.800E–04	0.346	2.242E–17	46.0
	5.171	4.940	1.880	1.647E–04	0.352	2.016E–17	45.1

Table T10. X-ray diffraction analysis, Site 1073.

Core, section, interval (cm)	Depth (mbsf)	Mineral (wt%)									
		Quartz	K-feldspar	Plagioclase	Calcite	Dolomite	Amphibole	Gypsum	Pyrite	Clay	Total
174A-1073A-											
8H-1, 17–22	63.75	29	04	12	12	08	01	00	TR	34	100
16H-3, 135–150	143.95	38	05	19	11	02	01	00	01	23	100
26X-2, 76–82	226.65	38	05	19	00	01	01	01	01	34	100
41X-5, 97–103	372.35	30	05	20	13	03	02	00	TR	27	100
51X-1, 22–37	459.52	29	07	33	05	03	05	01	03	14	100
58X-6, 15–30	532.45	39	02	04	08	00	00	01	03	43	100
71X-1, 2–8	644.70	21	02	01	26	00	00	TR	02	48	100

Note: TR = phase present in abundance <0.5 wt%.

Table T11. SEM analysis, Site 1073.

Core, section, interval (cm)	Depth (mbsf)	Quartz	K-feldspar	Plagioclase	Calcite	Dolomite	Amphibole	Gypsum	Pyrite	Smectite	Illite	Glauconite*	Total
174-1073A-													
8H-1, 17-22	63.75	15	03	04	0.5	03	05	00	0.2	45.5	15.4	2.0	93.6
71X-1, 2-8	644.70	09	01	01	1.4	00	0.6	00	1.4	12.4	31.8	40.5	99.1

Note: * = XRD does not recognize glauconite.

Figure AF1. Thin section images from physical properties samples.

Sample 174A-1073A-14H-2, 99-101 cm

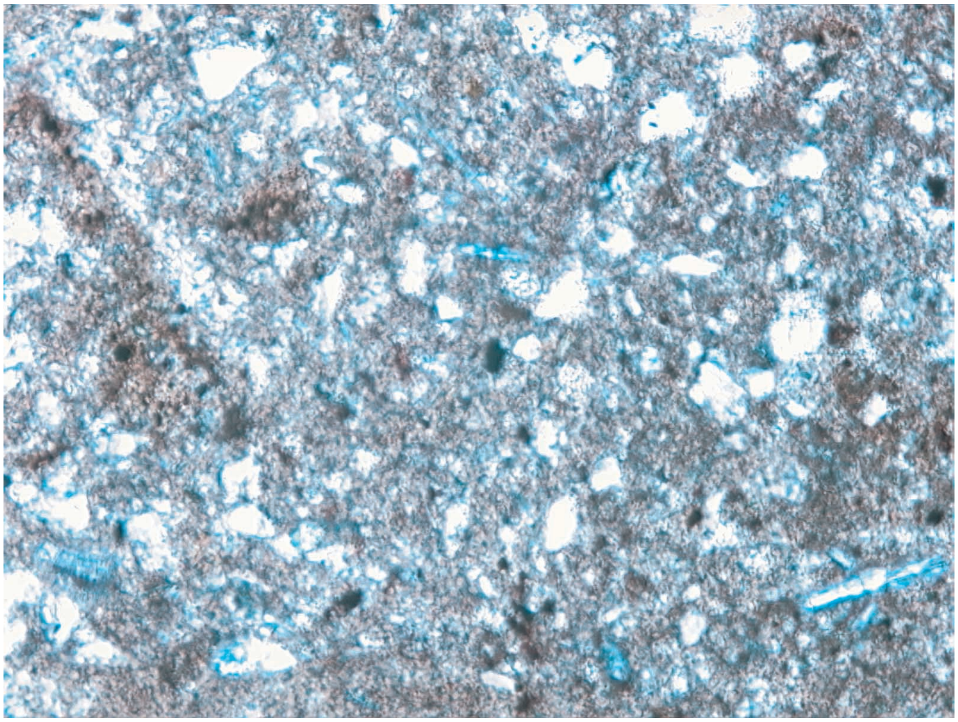

0.1 mm

Sample 174A-1073A-16H-4, 101-103 cm

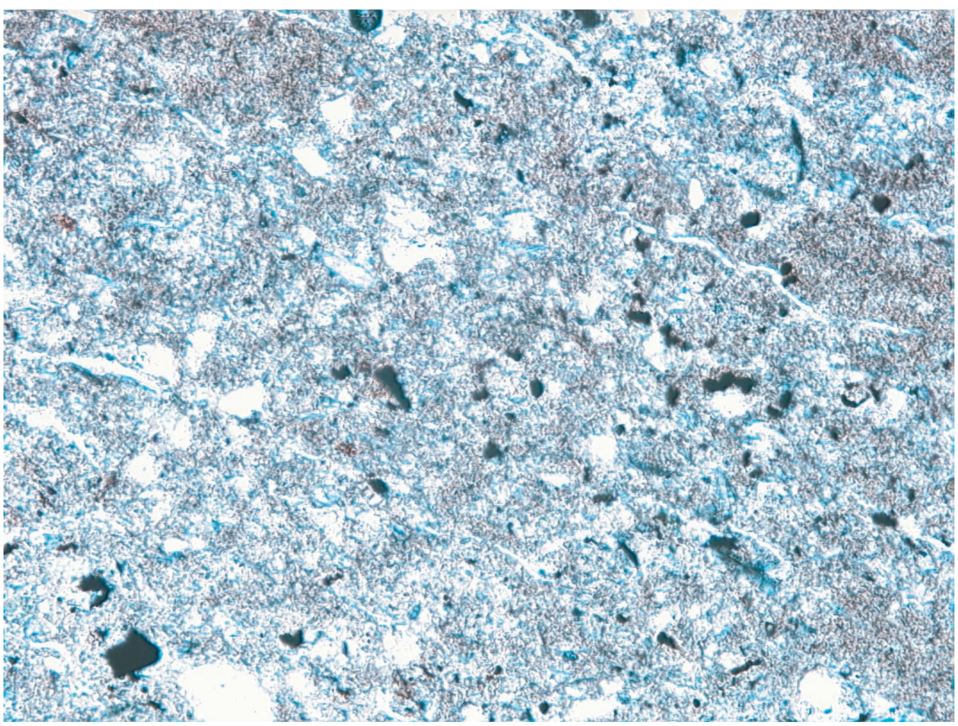

0.1 mm

Figure AF2. Thin section images from physical properties samples.

Sample 174A-1073A-20H-2, 143-145 cm

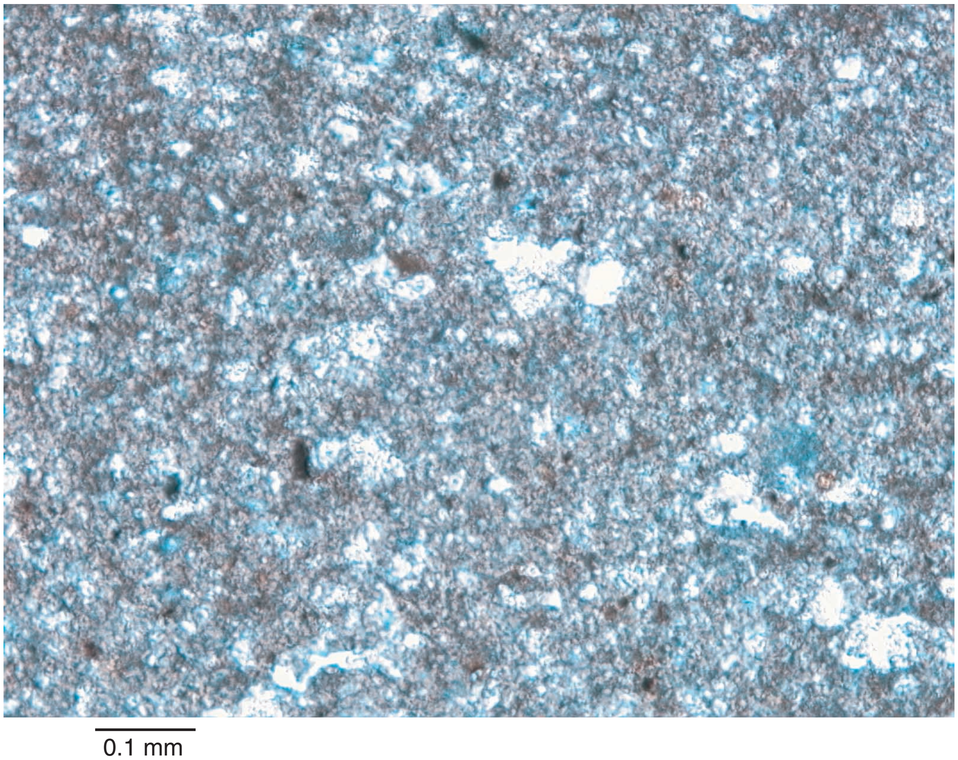

Sample 174A-1073A-27X-4, 117-119 cm

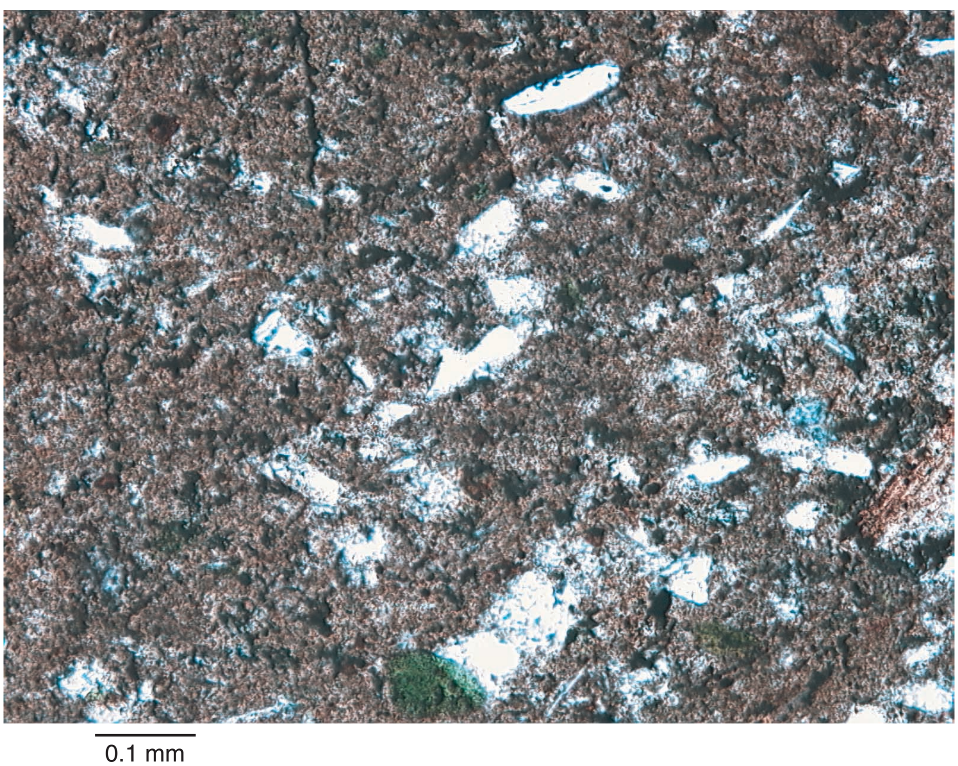

Figure AF3. Thin section images from physical properties samples.

Sample 174A-1073A-34X-6, 26-28 cm

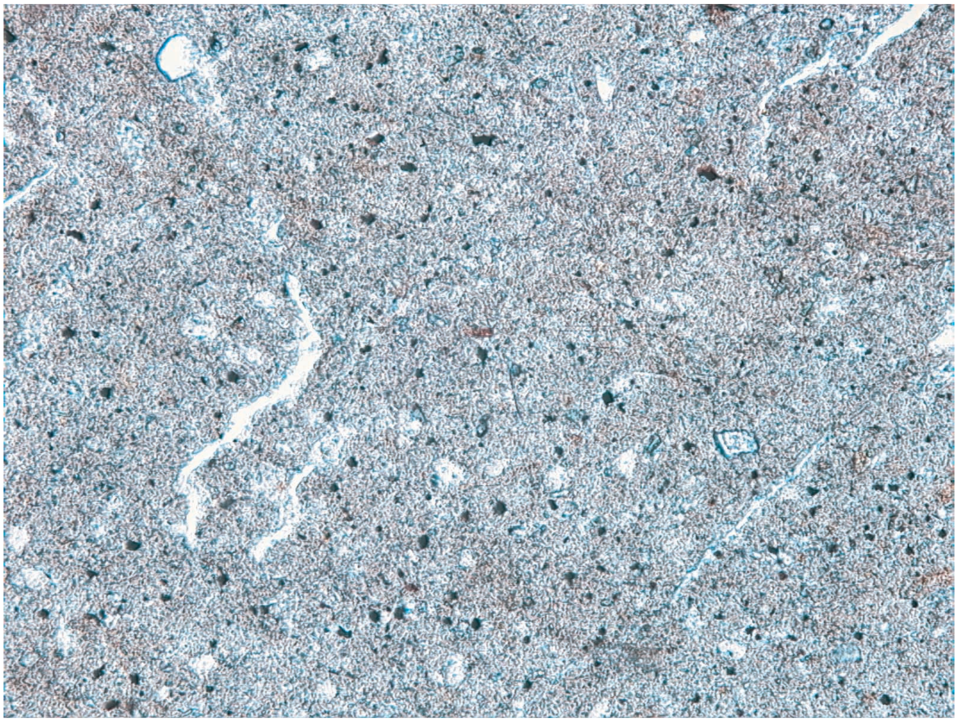

0.1 mm

Sample 174A-1073A-41X-2, 50-52 cm

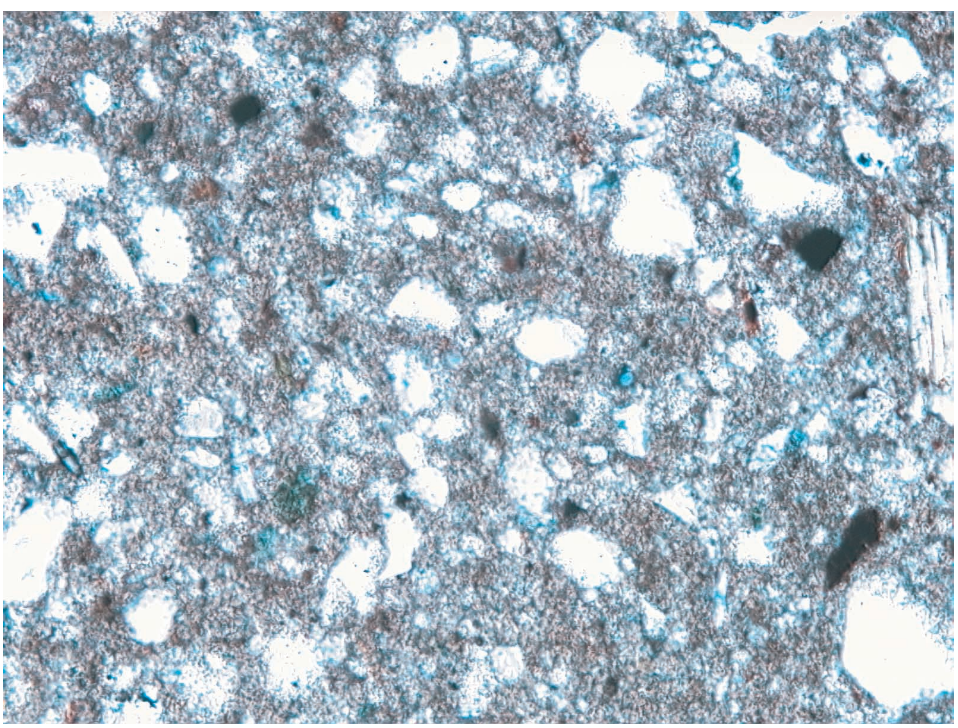

0.1 mm

Figure AF4. Thin section images from physical properties samples.

Sample 174A-1073A-41X-5, 50-52 cm

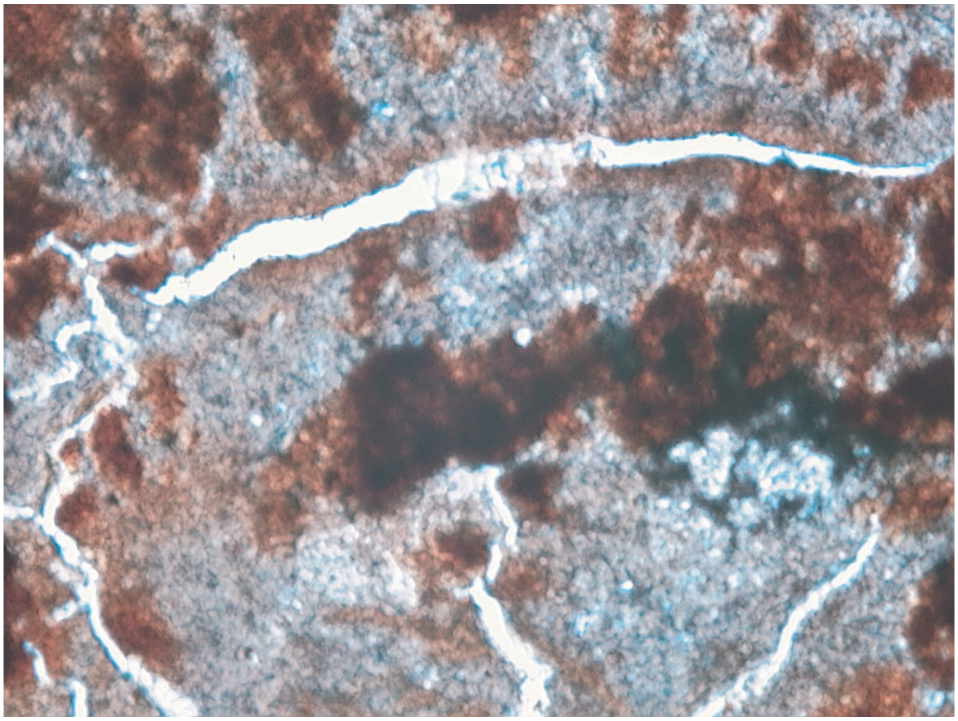

0.1 mm

Sample 174A-1073A-44X-5, 13-15 cm

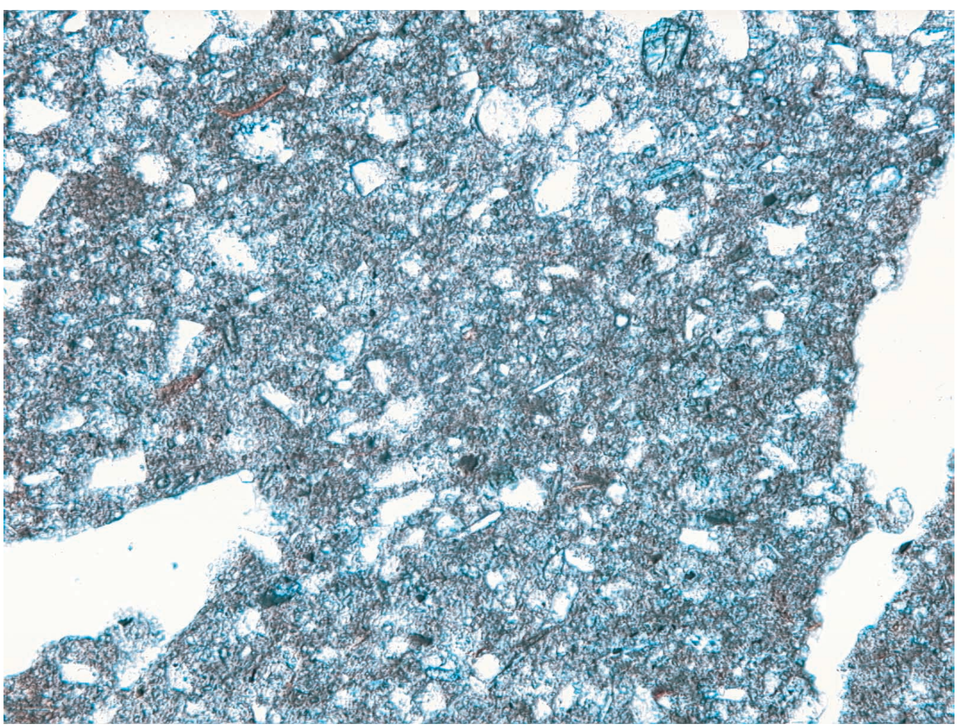

0.1 mm

Figure AF5. Thin section images from physical properties samples.

Sample 174A-1073A-50X-5, 86-88 cm

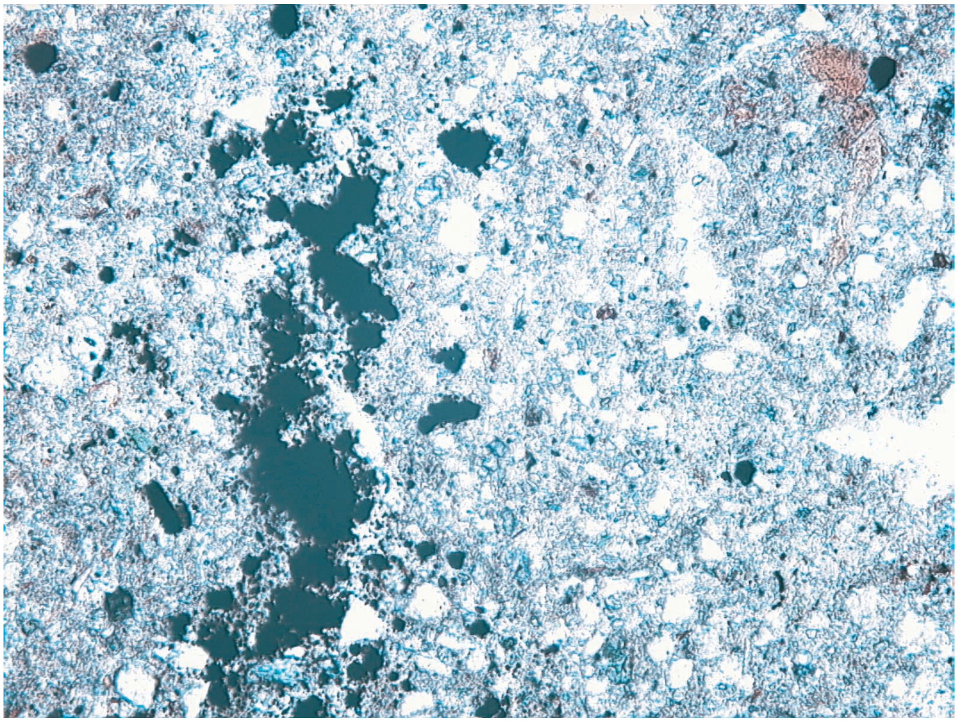

0.1 mm

Sample 174A-1073A-56X-2, 97-99 cm

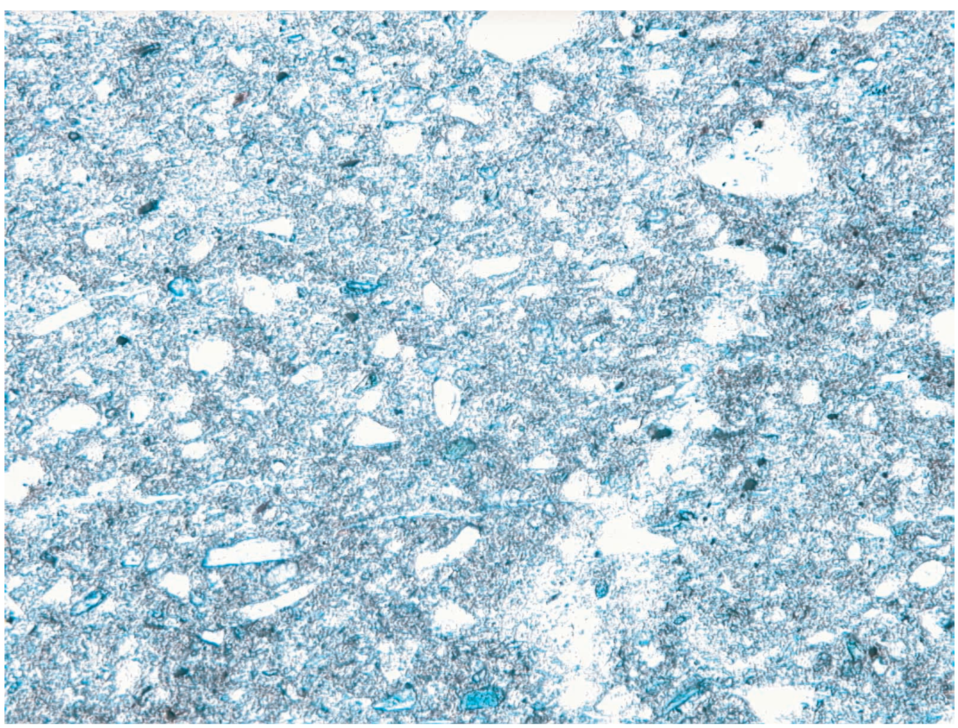

0.1 mm

Figure AF6. Thin section images from physical properties samples.

Sample 174A-1073A-59X-1, 62-64 cm

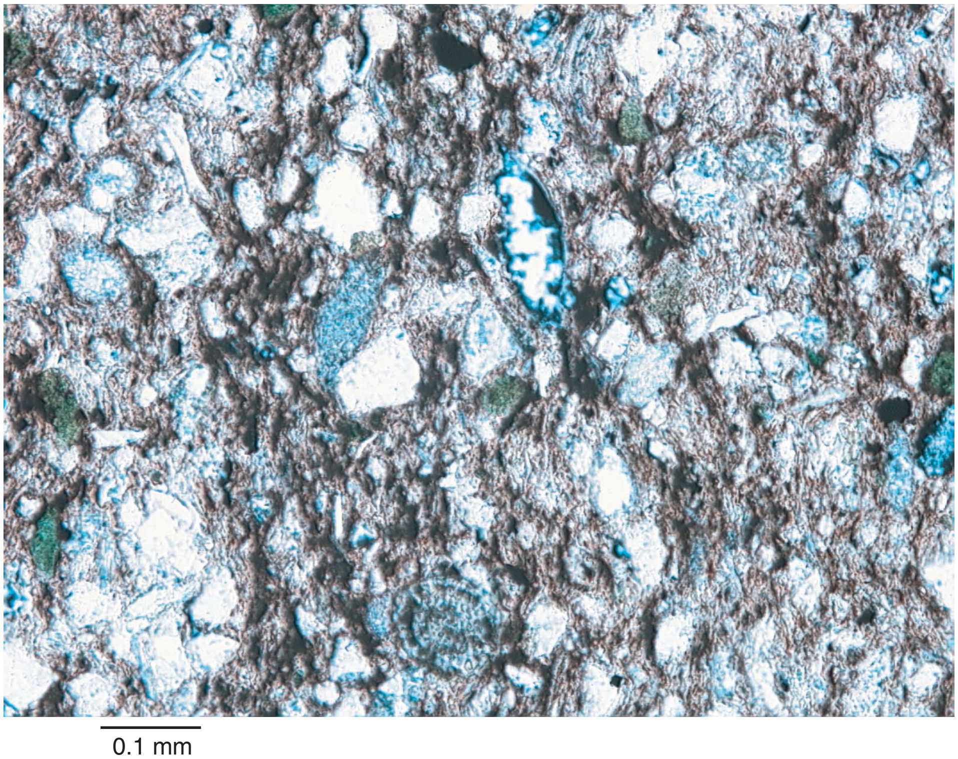

Sample 174A-1073A-60X-3, 43-45 cm

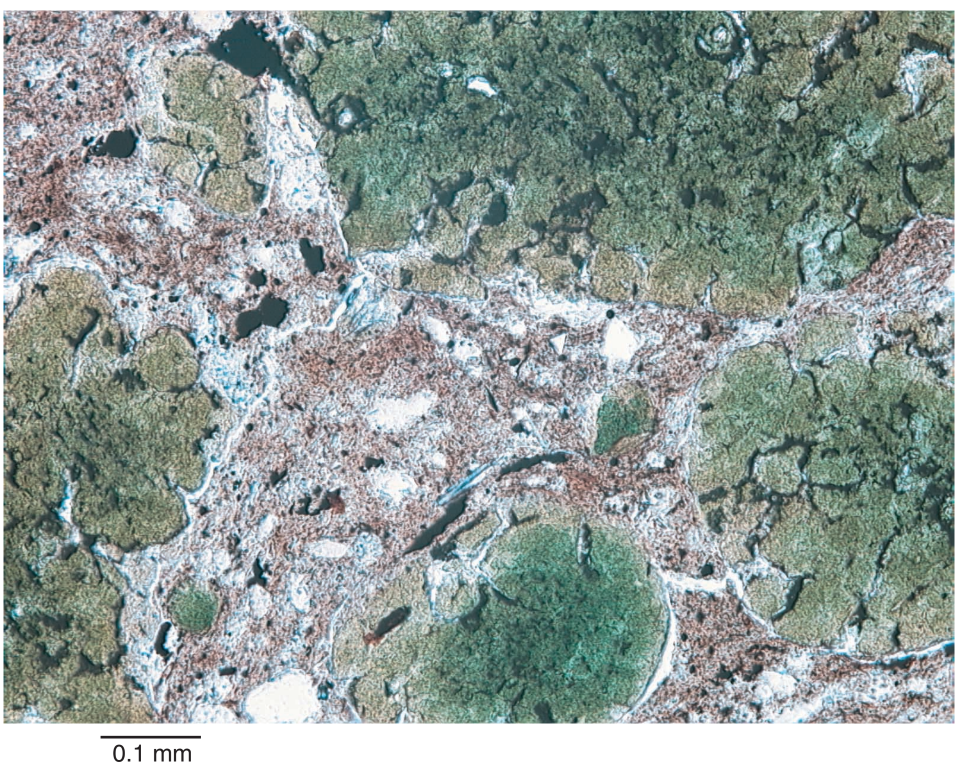

Figure AF7. Thin section images from physical properties samples.

Sample 174A-1073A-60X-6, 47-49 cm

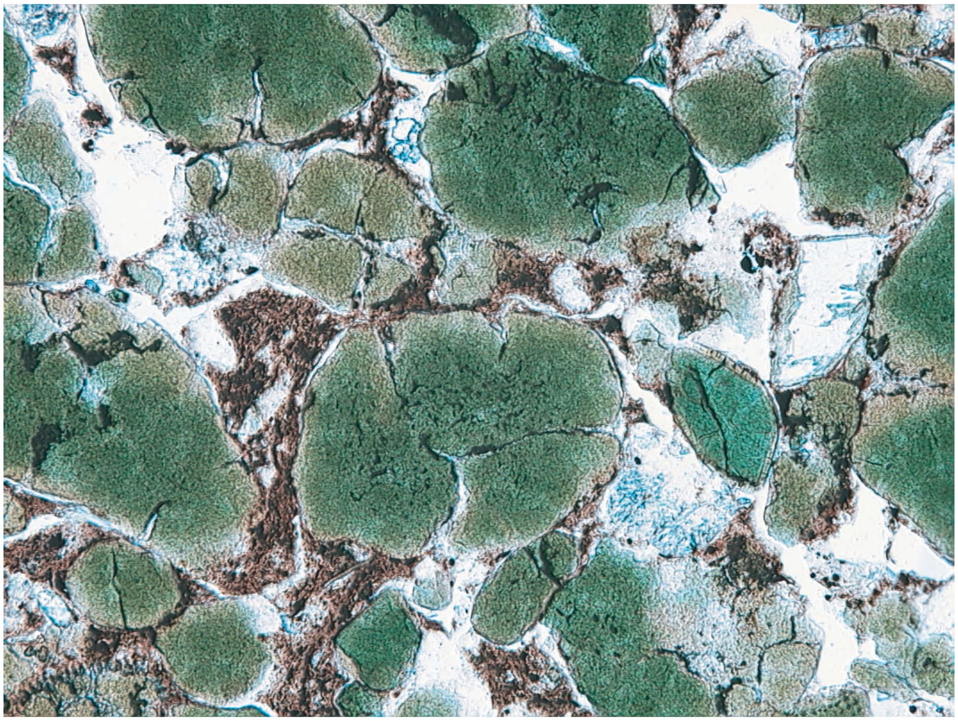

0.1 mm

Sample 174A-1073A-62X-2, 110-112 cm

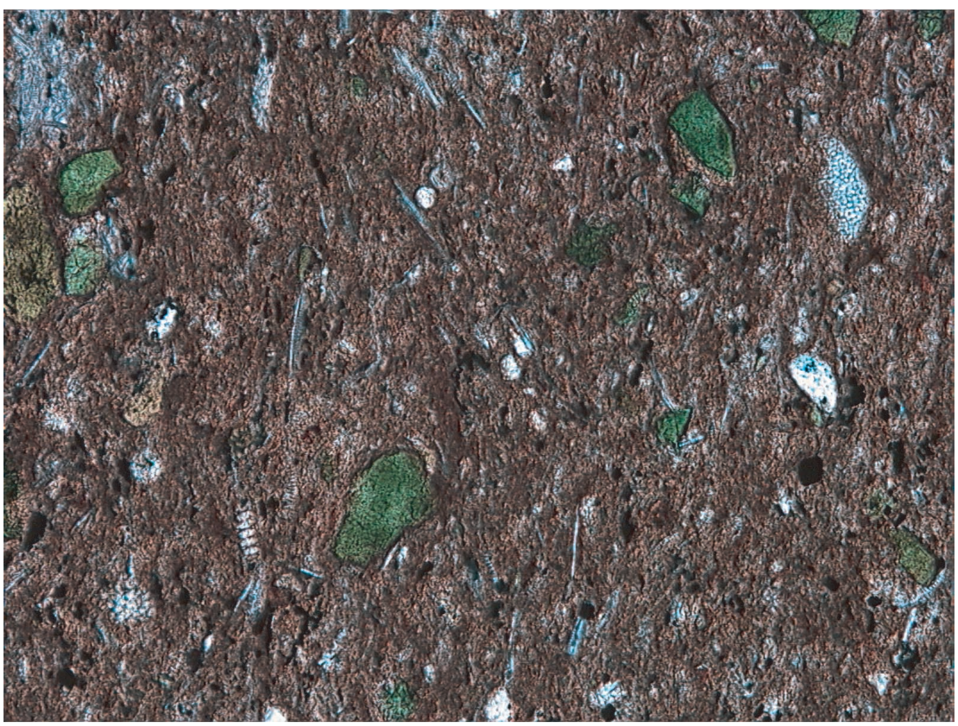

0.1 mm

Figure AF8. Thin section images from physical properties samples.

Sample 174A-1073A-62X-5, 122-124 cm

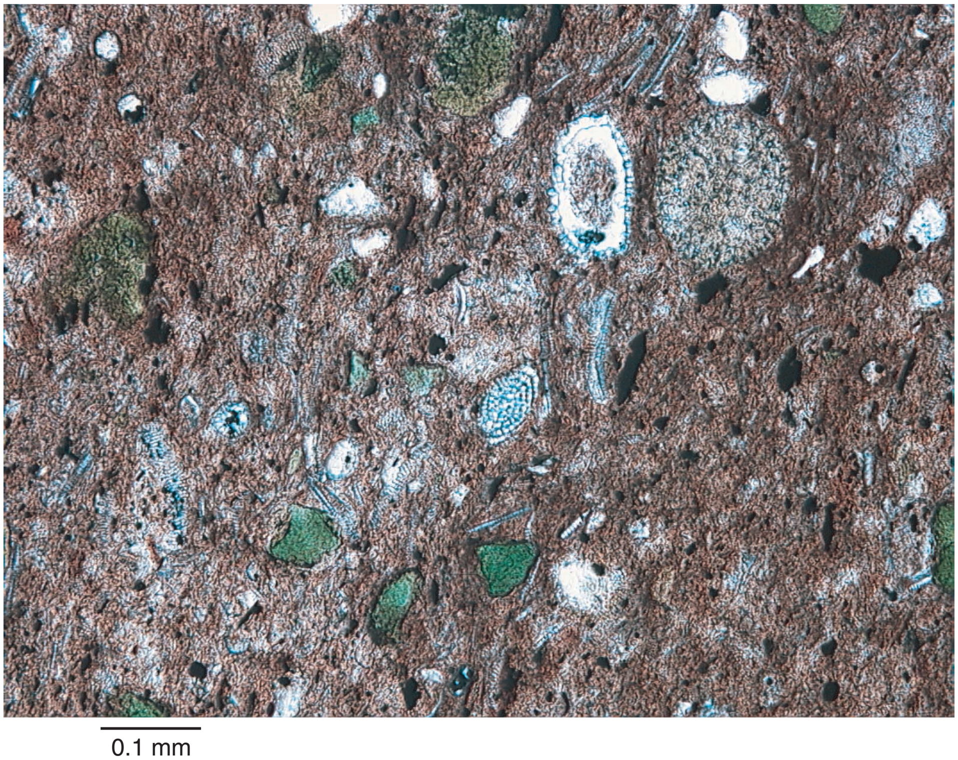

Sample 174A-1073A-66X-2, 130-132 cm

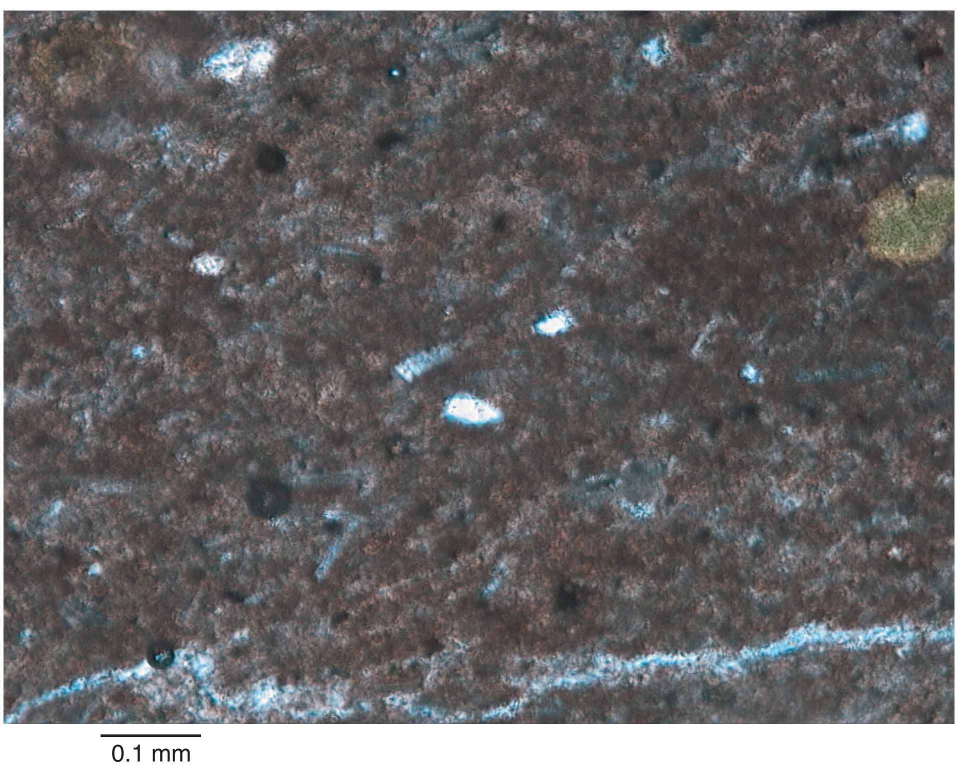

Figure AF9. Thin section images from physical properties samples.

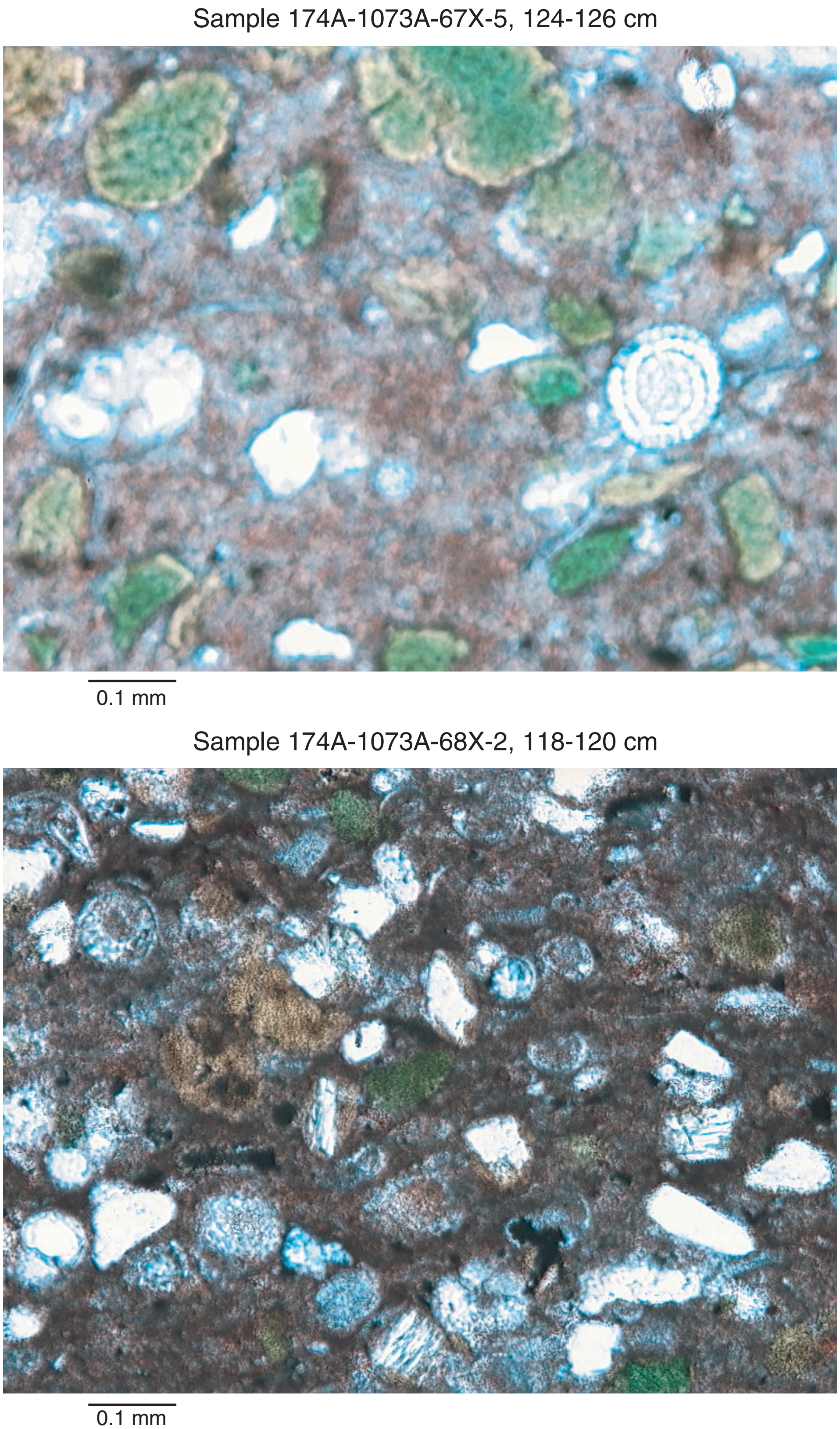

Figure AF10. Thin section images from physical properties samples.

Sample 174A-1073A-68X-5, 113-115 cm

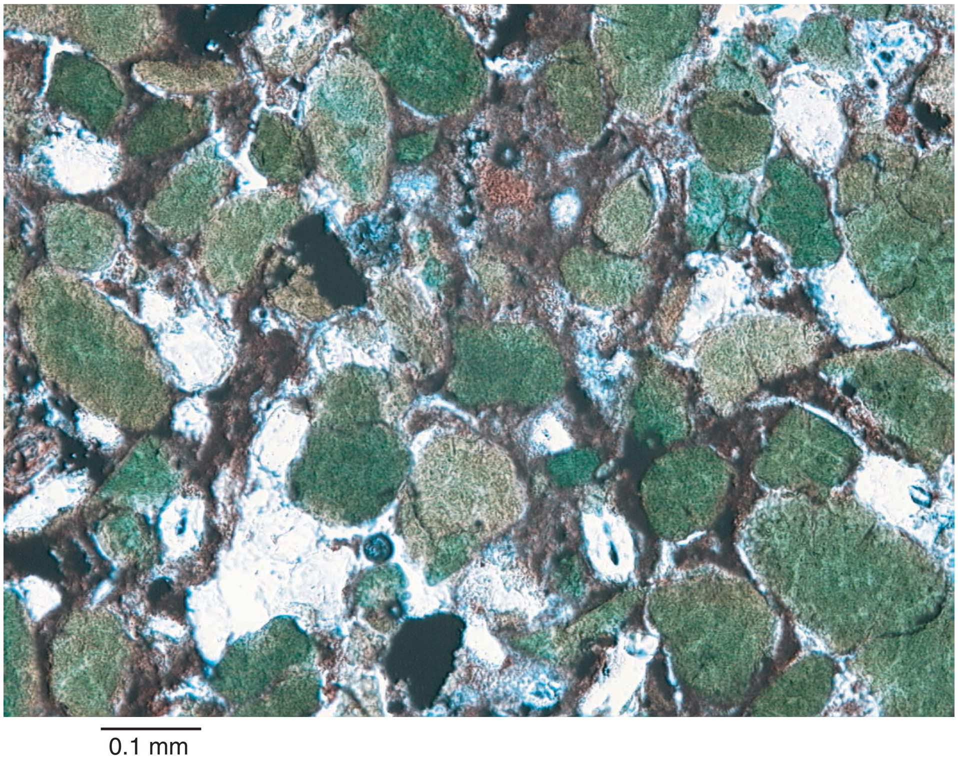

Sample 174A-1073A-69X-2, 133-135 cm

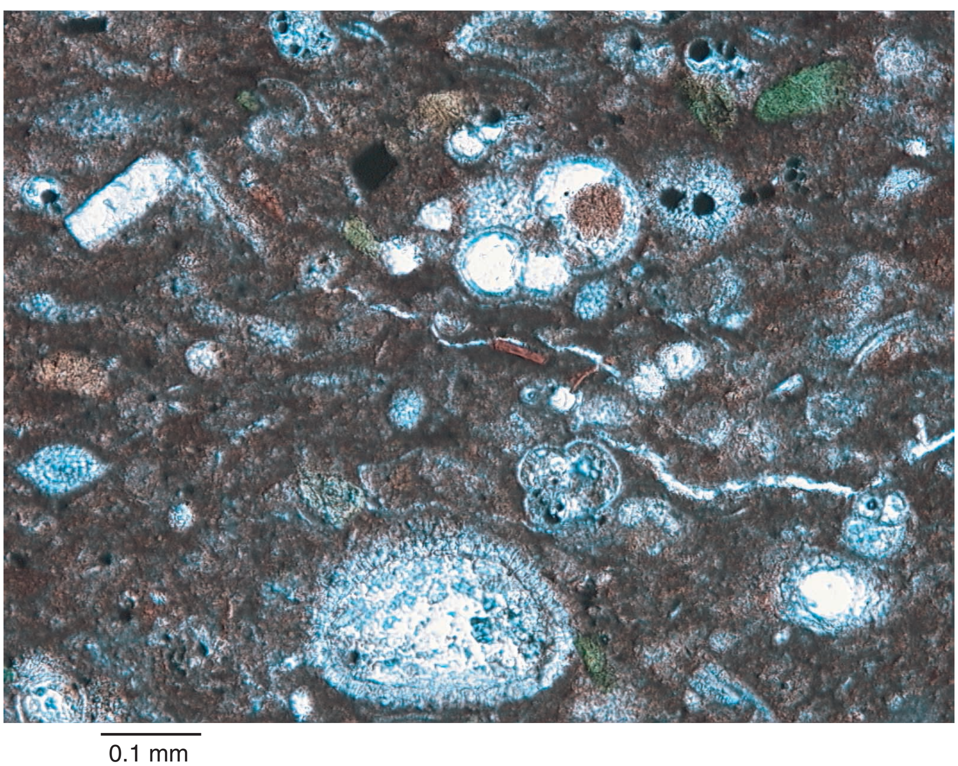

Figure AF11. Thin section image from whole core. Black boxes identify regions analyzed by SEM. Numbers identify SEM image(s) for that region.

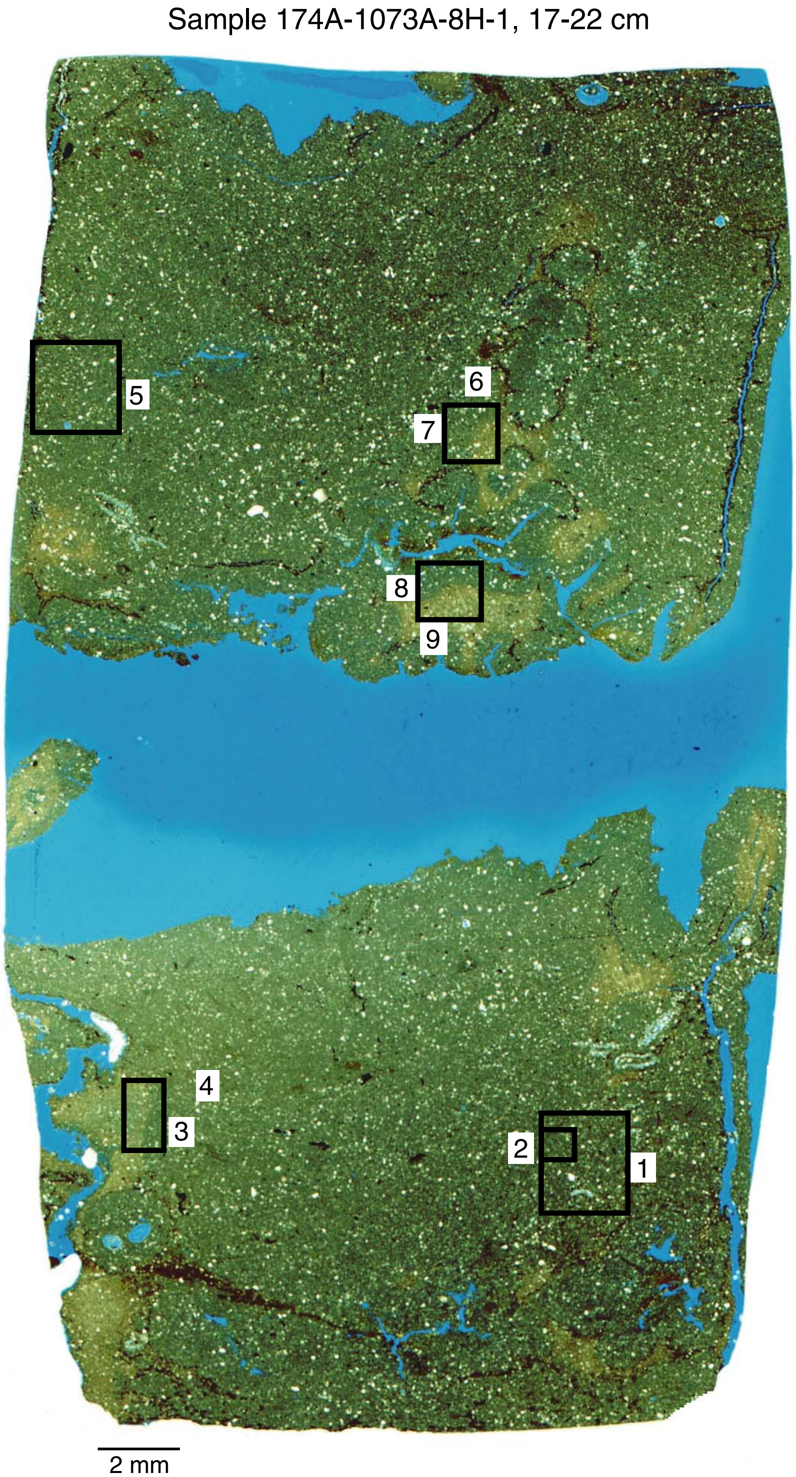

Figure AF12. Thin section image from whole core.

Figure AF13. Thin section image from whole core.

Figure AF14. Thin section image from whole core.

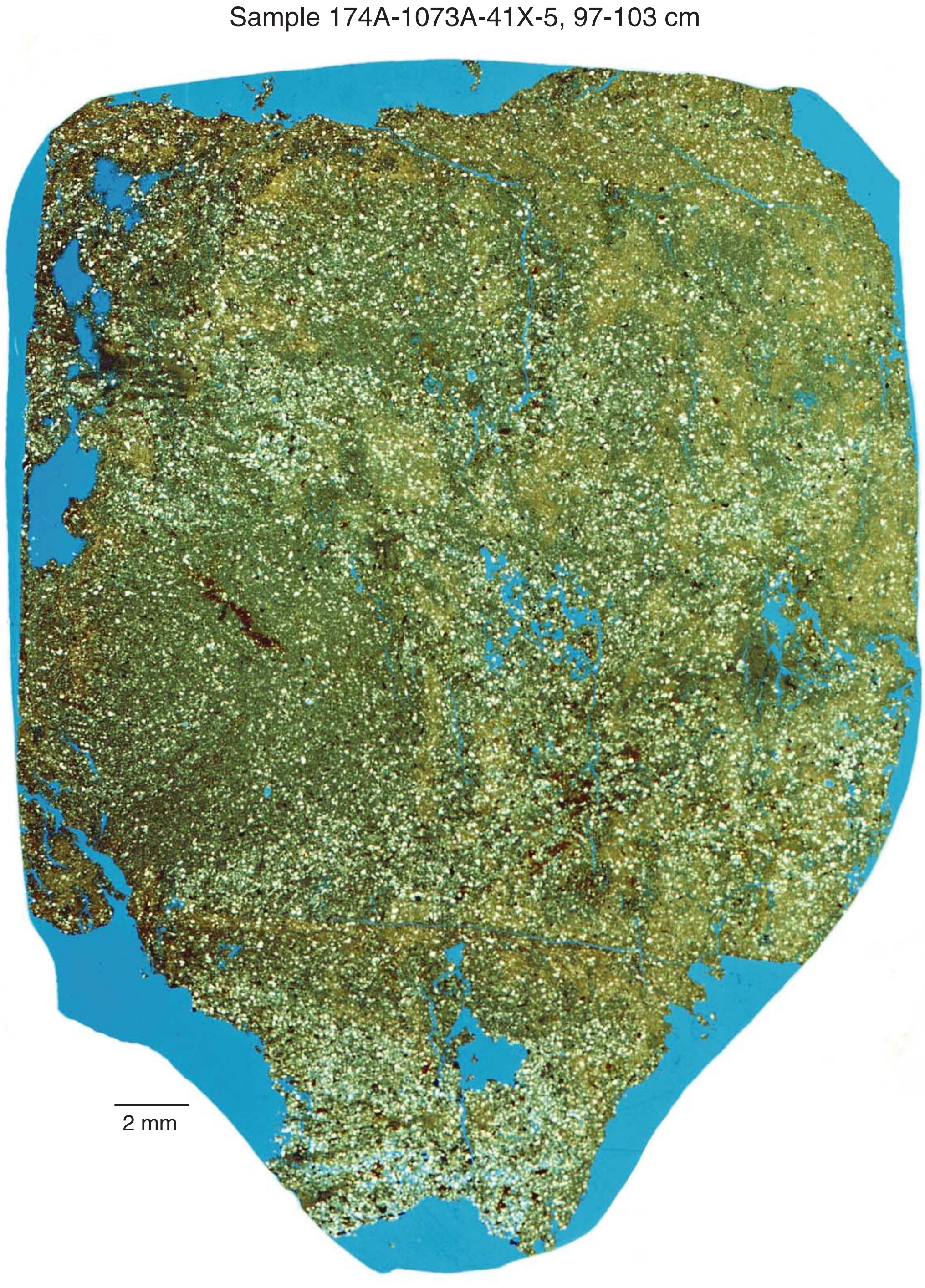

Figure AF15. Thin section image from whole core.

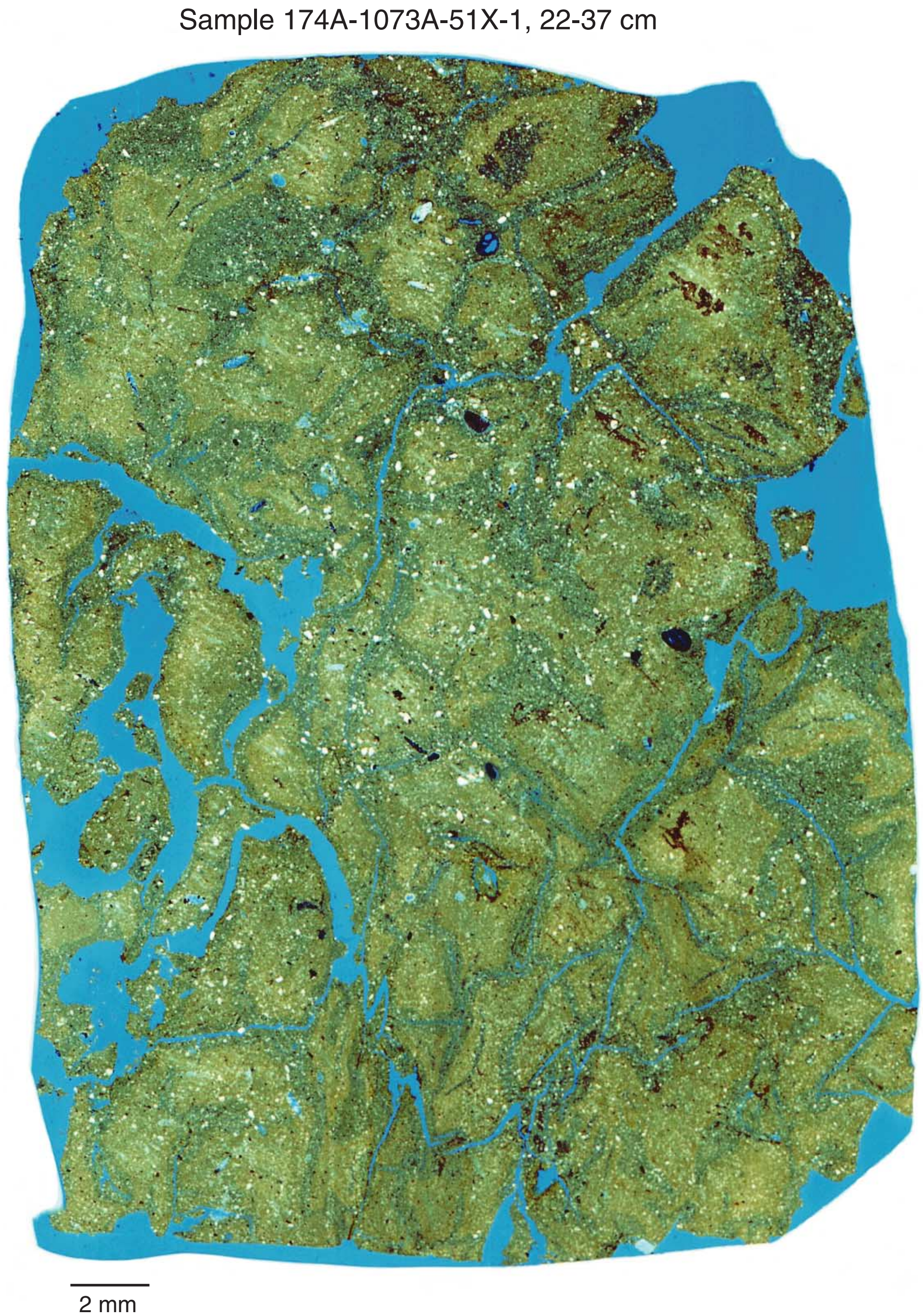

Figure AF16. Thin section image from whole core. Black boxes identify regions analyzed by SEM. Numbers identify SEM image(s) for that region.

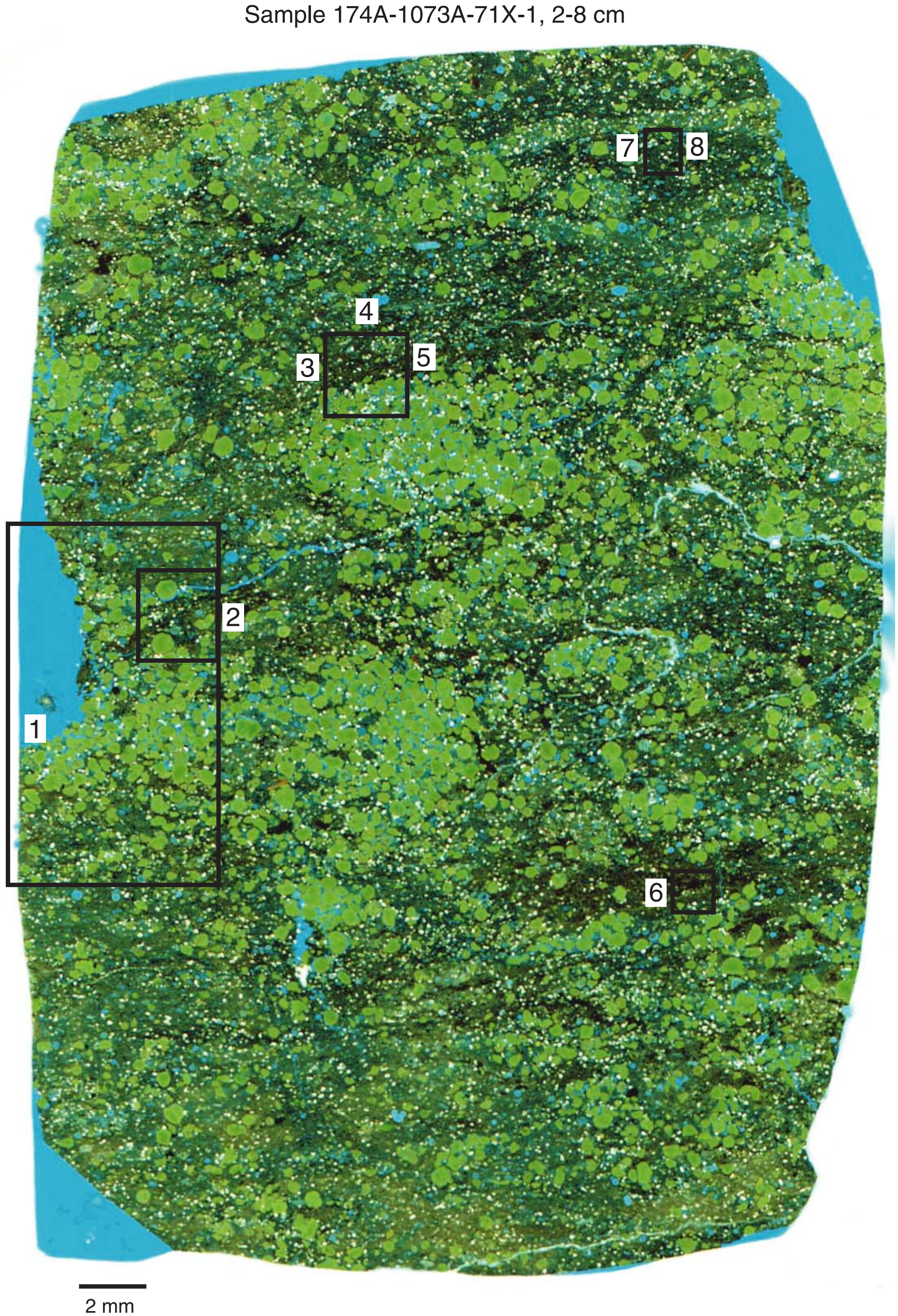

Figure AF17. SEM image at 72×. Q = quartz, Py = pyrite, Px = pyroxene, Dolo = dolomite.

Sample 174A-1073A-8H-1, 17-22 cm SEM 1

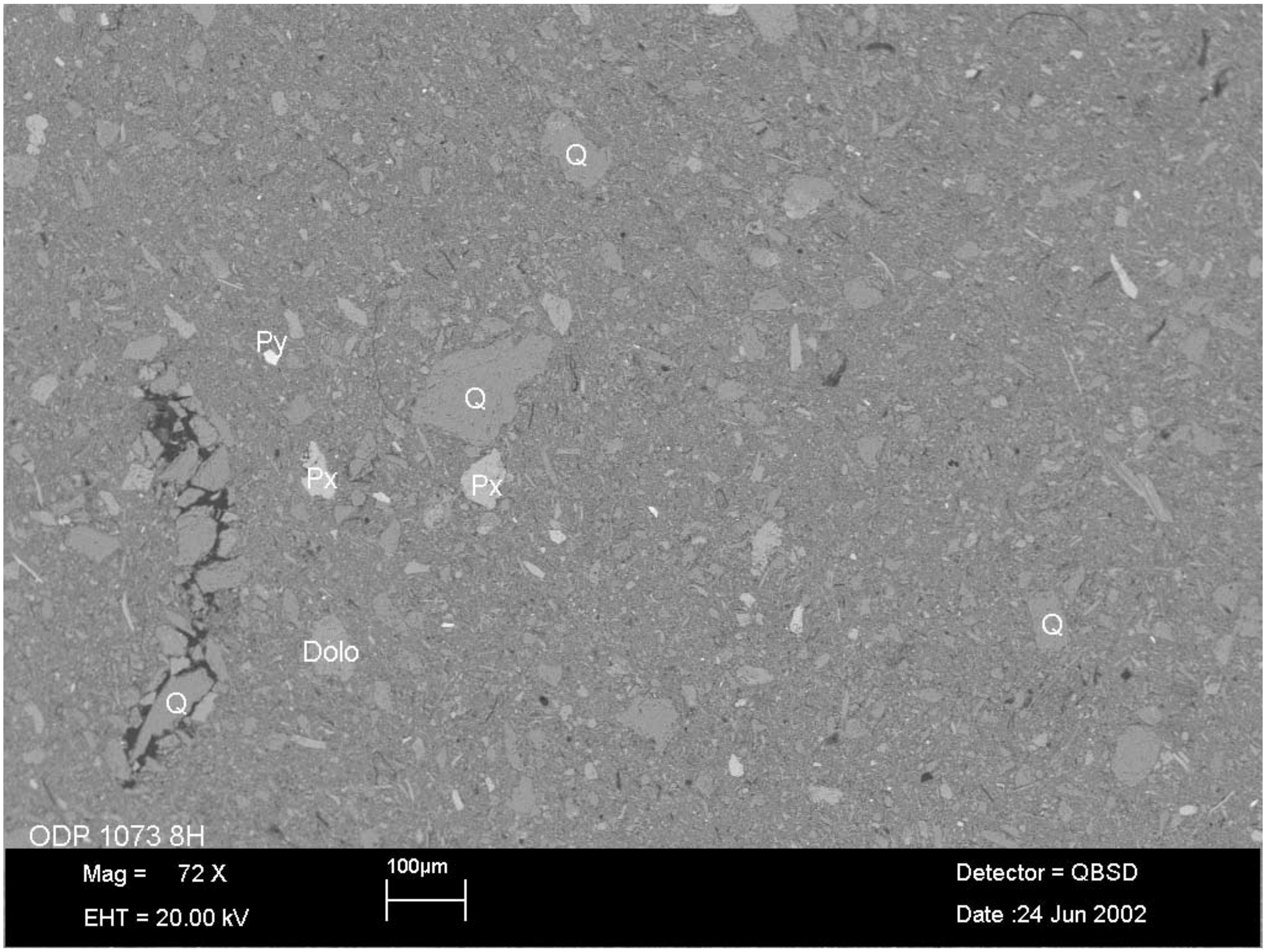

Figure AF18. SEM image at 400×. Q = quartz, Bio = biotite, Plag = plagioclase, Ab = albite.

Sample 174A-1073A-8H-1, 17-22 cm SEM 2

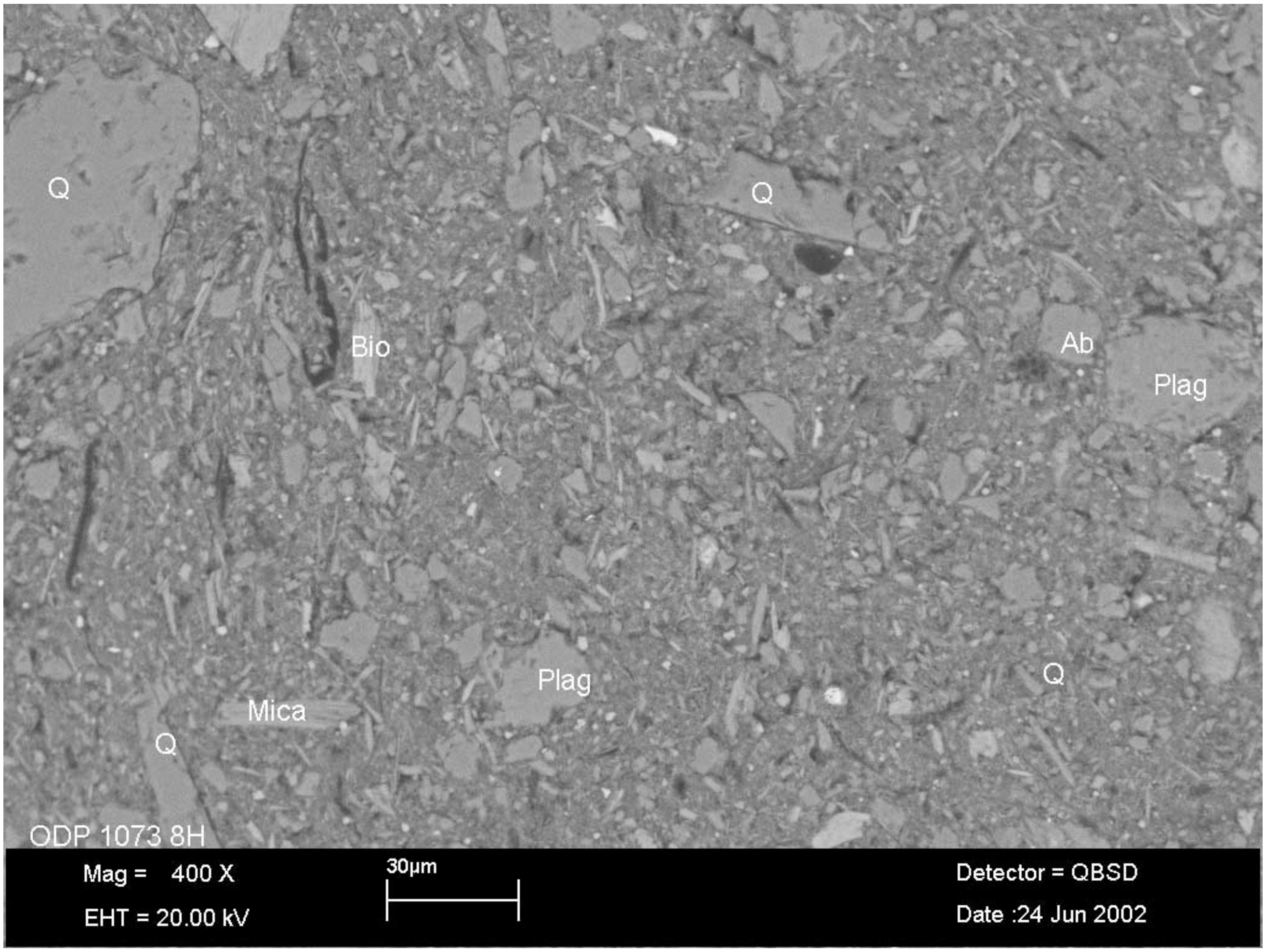

Figure AF19. SEM image at 62×.

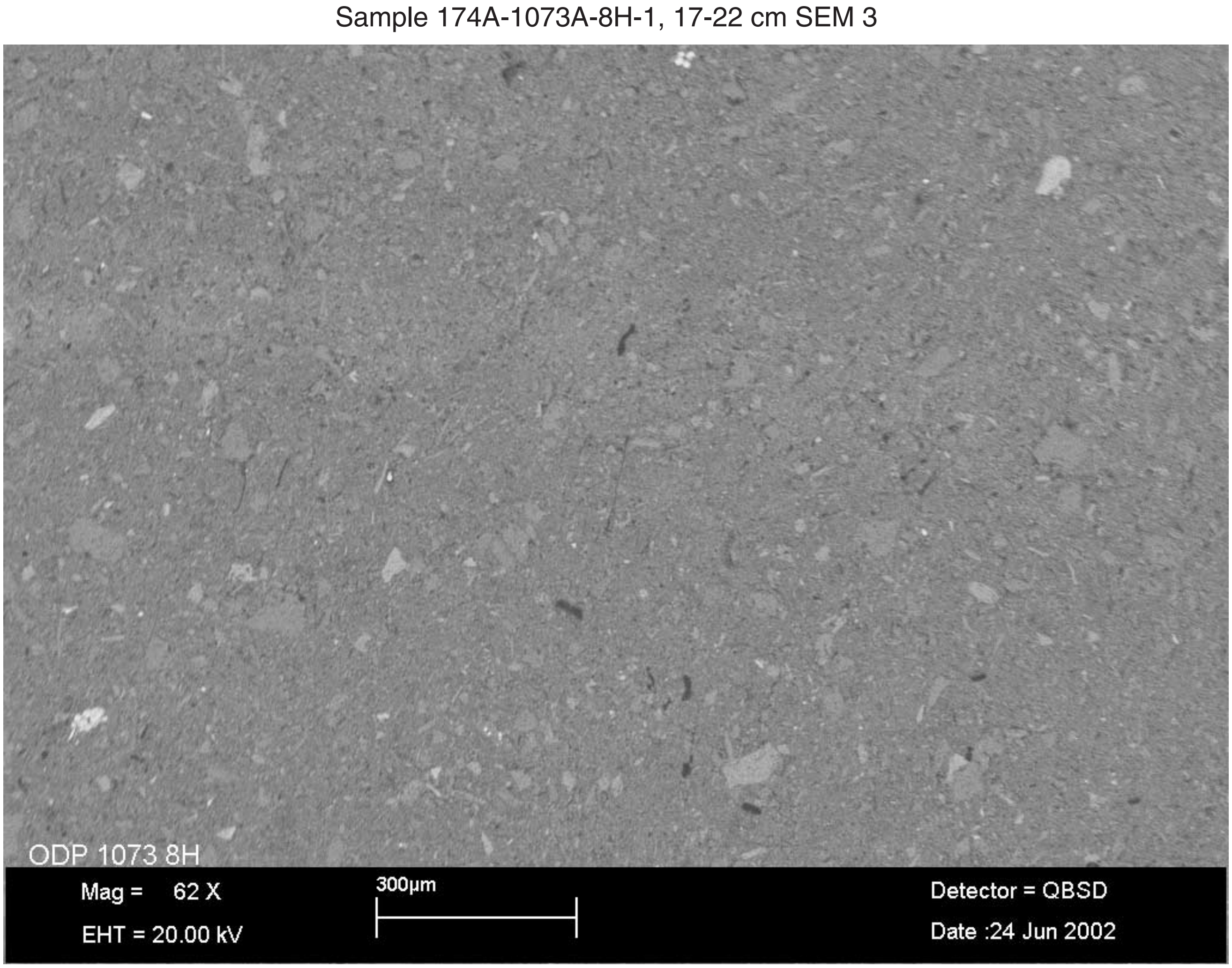

Figure AF20. SEM image at 1130×.

Sample 174A-1073A-8H-1, 17-22 cm SEM 4

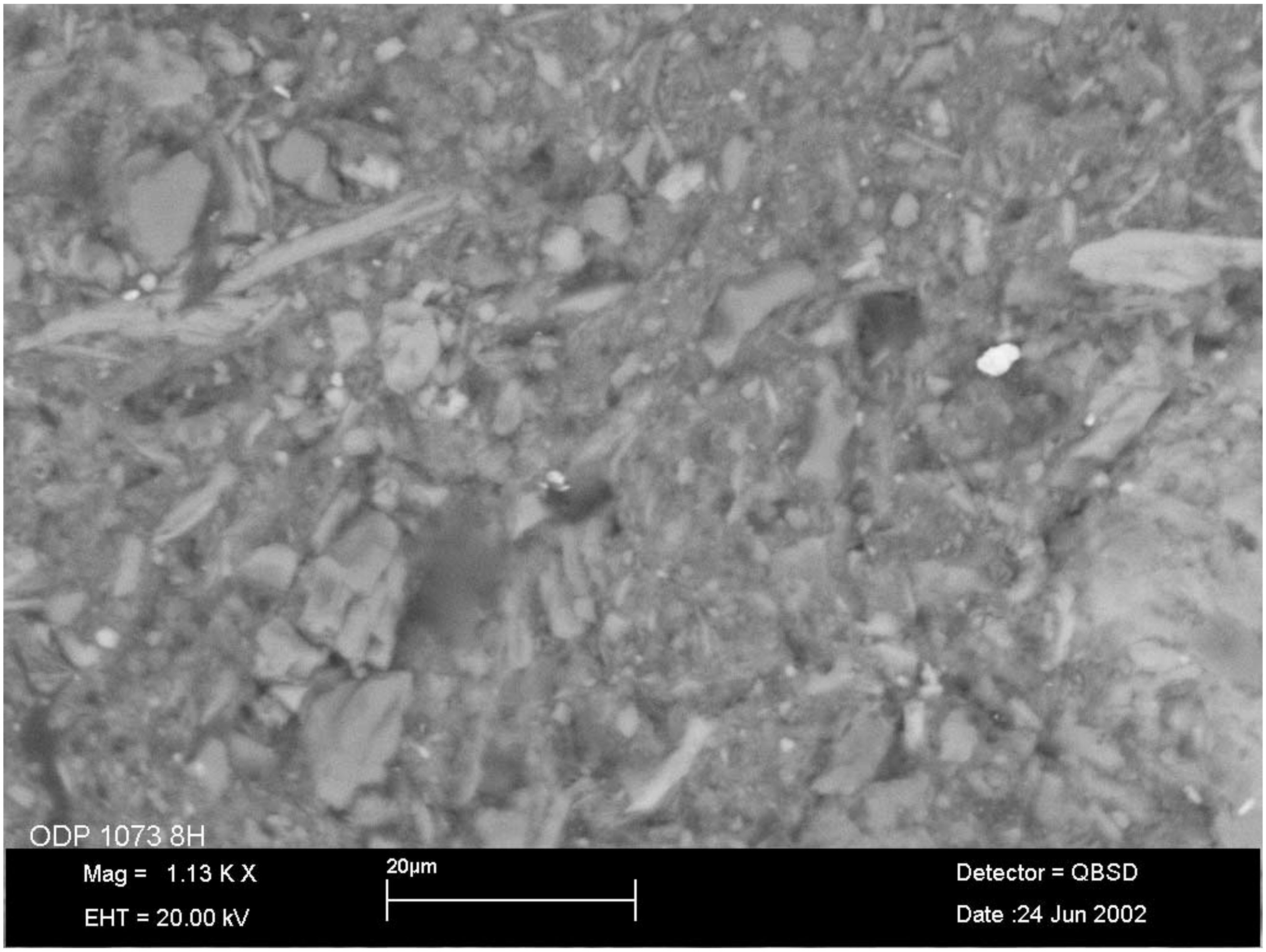

Figure AF21. SEM image at 60×.

Sample 174A-1073A-8H-1, 17-22 cm SEM 5

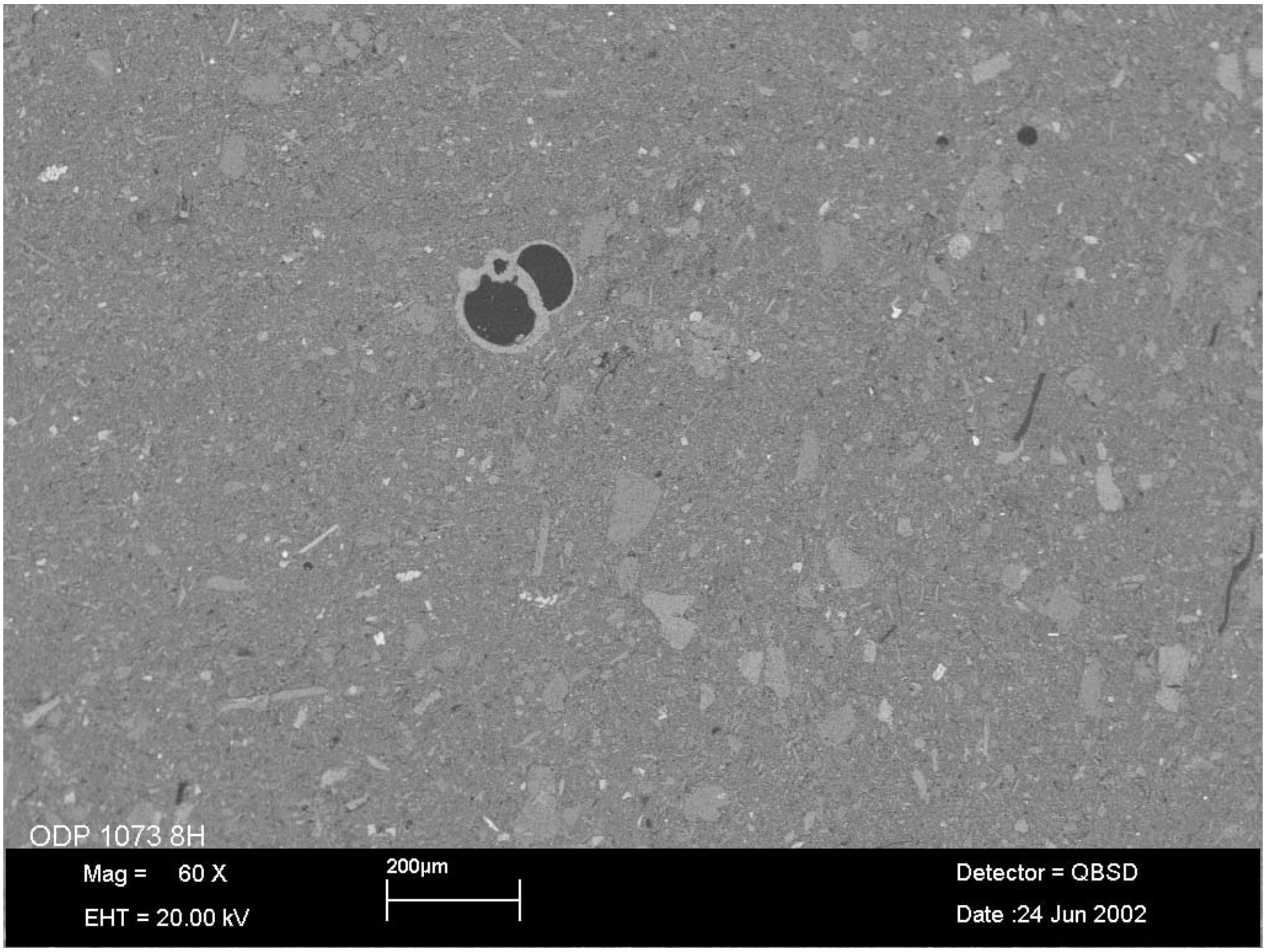

Figure AF22. SEM image at 63×.

Sample 174A-1073A-8H-1, 17-22 cm SEM 6

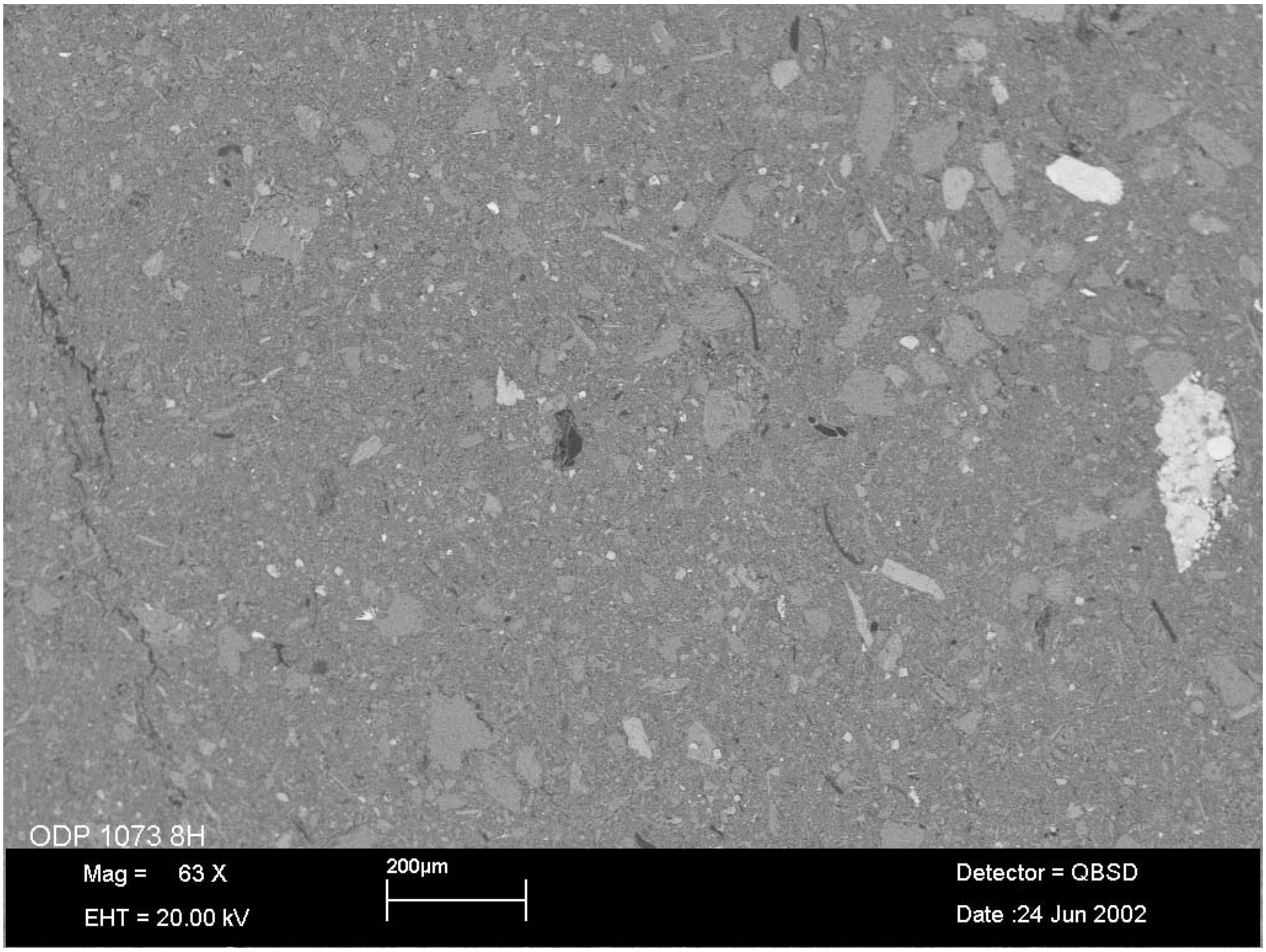

Figure AF23. SEM image at 450×. Il = illite, Q = quartz, Zr = zircon, Ab = albite.

Sample 174A-1073A-8H-1, 17-22 cm SEM 7

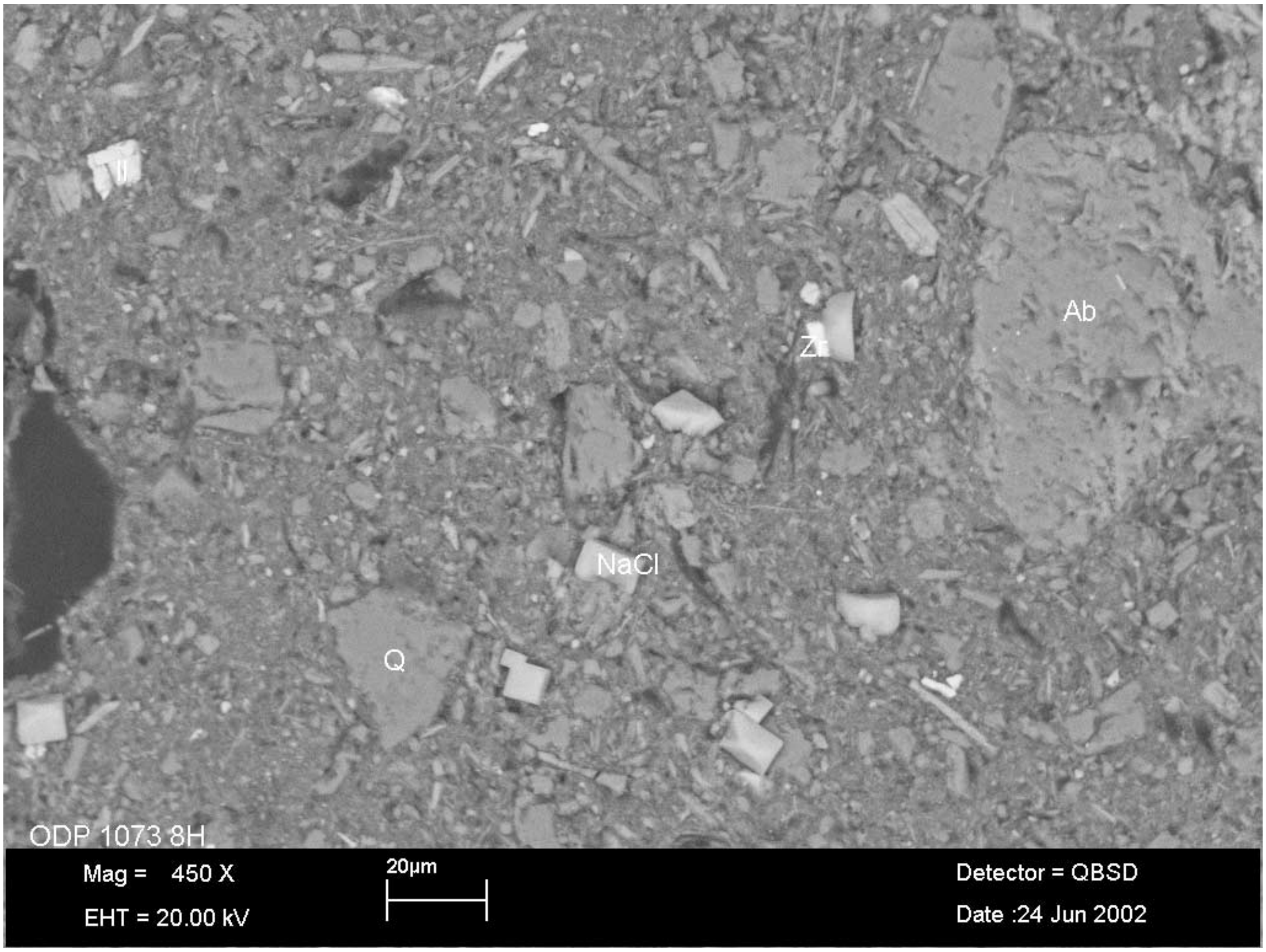

Figure AF24. SEM image at 72×.

Sample 174A-1073A-8H-1, 17-22 cm SEM 8

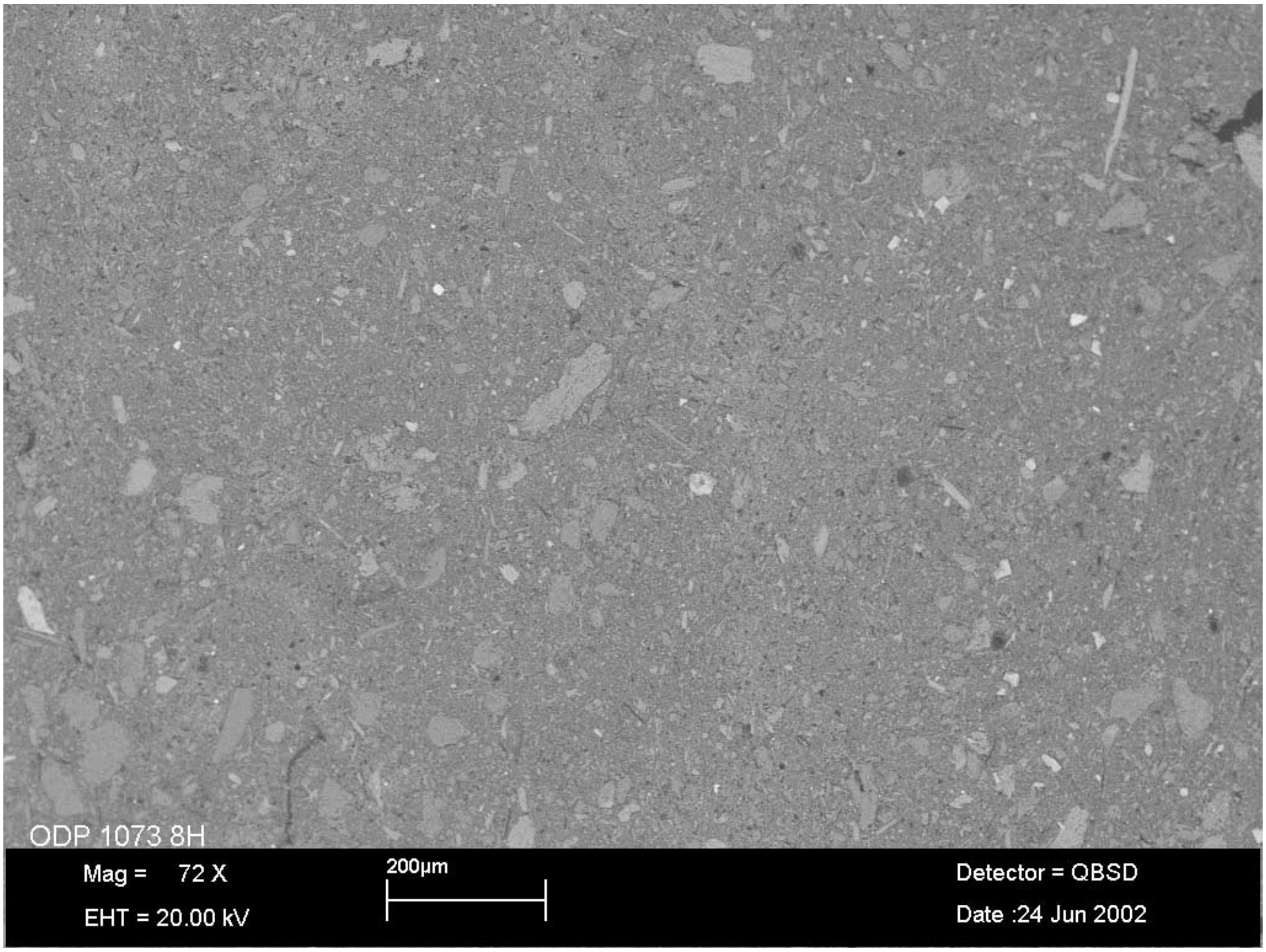

Figure AF25. SEM image at 600×. Q = quartz, Dolo = dolomite.

Sample 174A-1073A-8H-1, 17-22 cm SEM 9

Figure AF26. SEM image at 15×.

Sample 174A-1073A-71X-1, 2-8 cm SEM 1

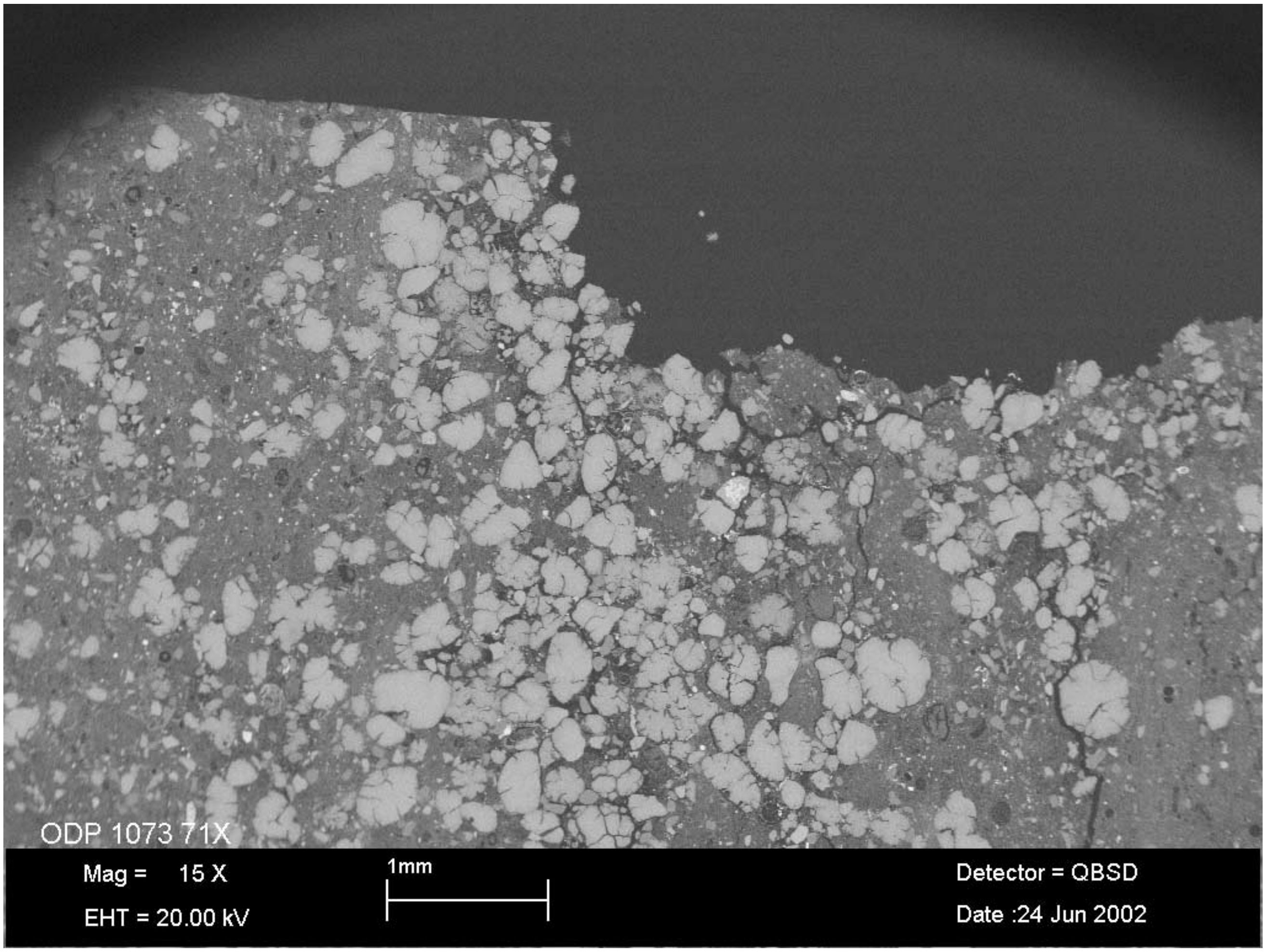

Figure AF27. SEM image at 60×. Py = pyrite, Gl = glauconite, KFel = K-feldspar, Zr = zircon, Ap = apatite, Plag = plagioclase.

Sample 174A-1073A-71X-1, 2-8 cm SEM 2

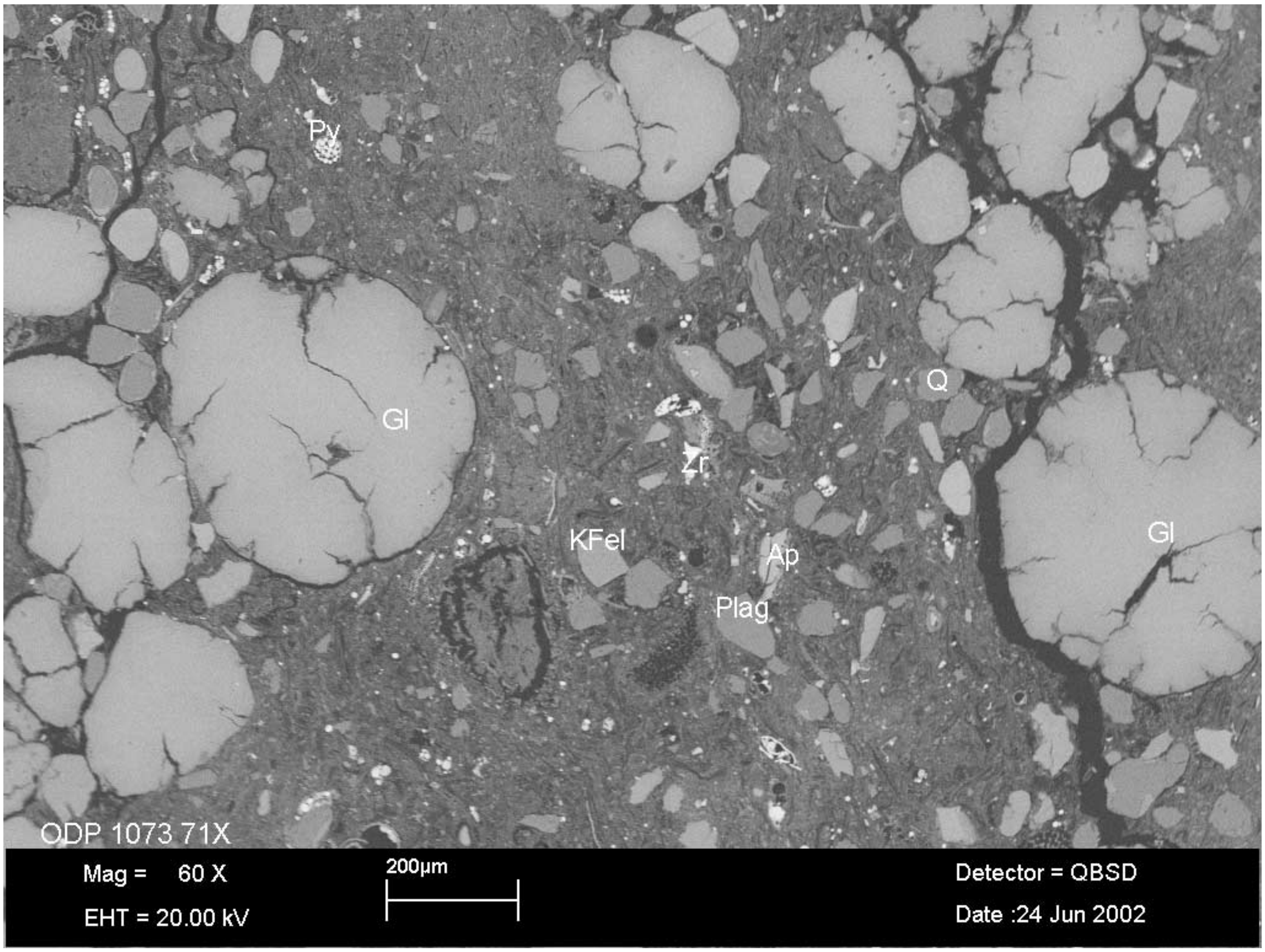

Figure AF28. SEM image at 15×. Gl = glauconite, Py = pyrite, Plag = plagioclase, Q = quartz.

Sample 174A-1073A-71X-1, 2-8 cm SEM 3

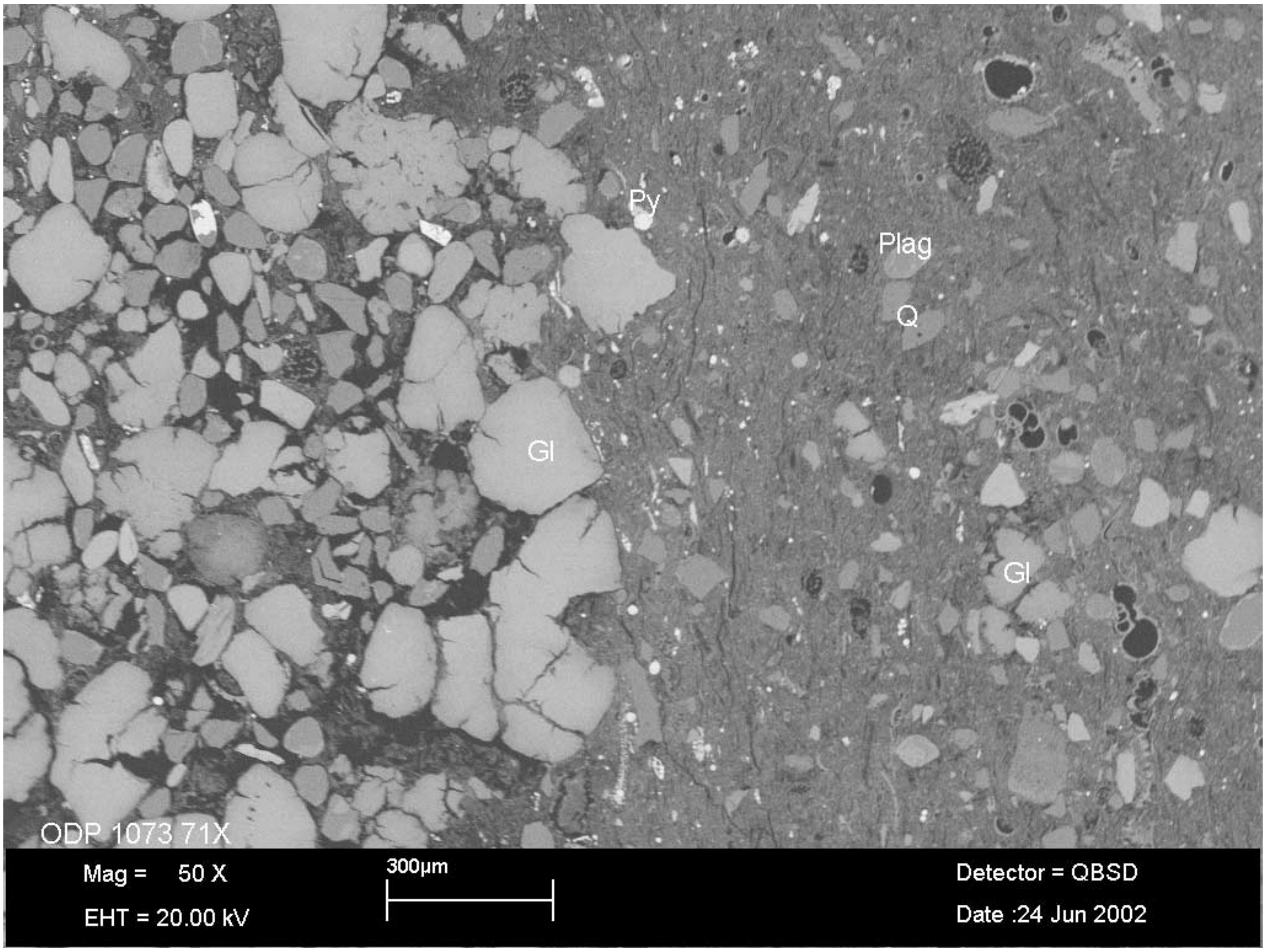

Figure AF29. SEM image at 300×. Gl = glauconite, KFel = K-feldspar, Q = quartz, Py = pyrite.

Sample 174A-1073A-71X-1, 2-8 cm SEM 4

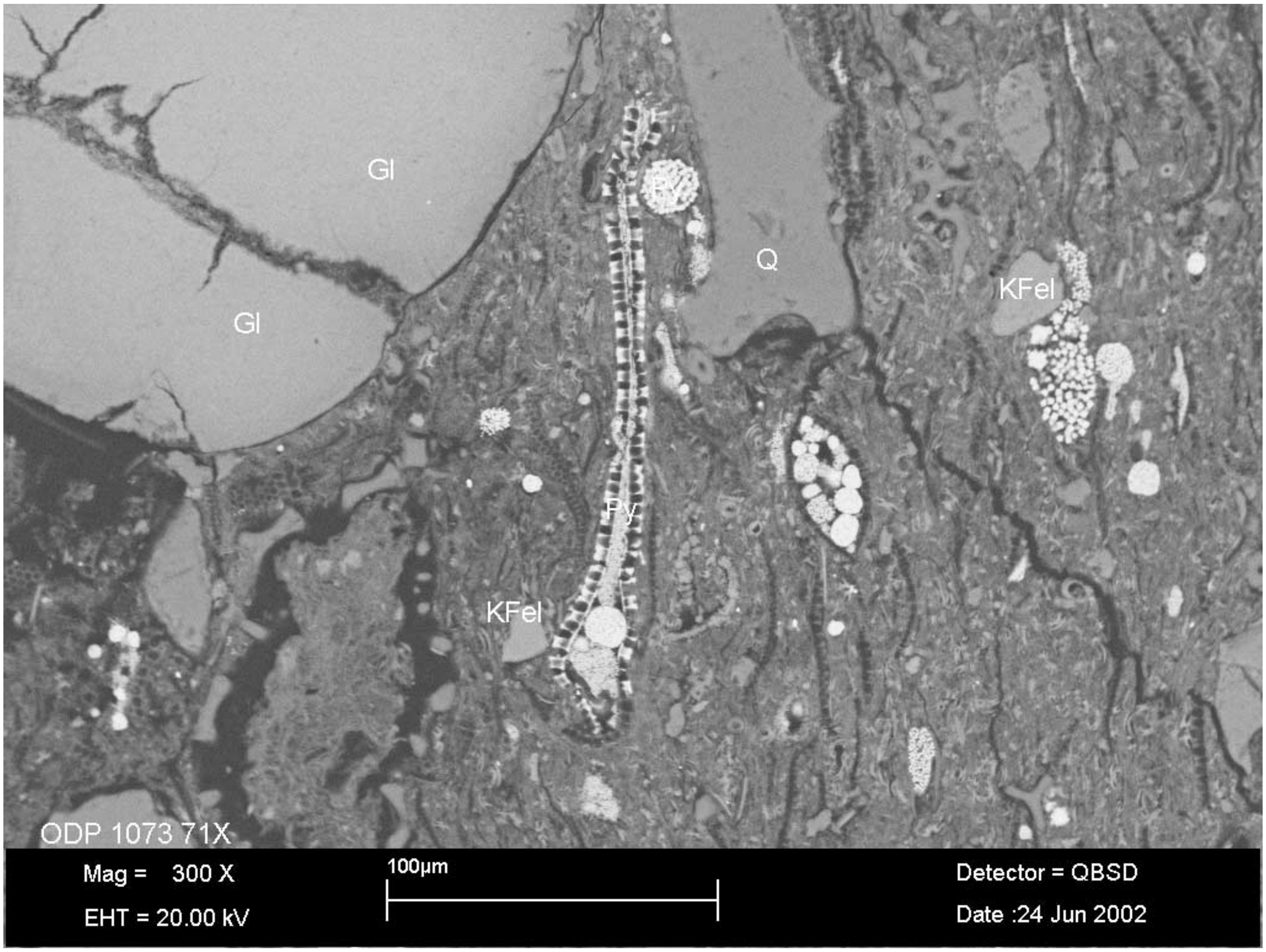

Figure AF30. SEM image at 335×. Py = pyrite, Q = quartz, Gl = glauconite, KFel = K-feldspar, Cal = calcite.

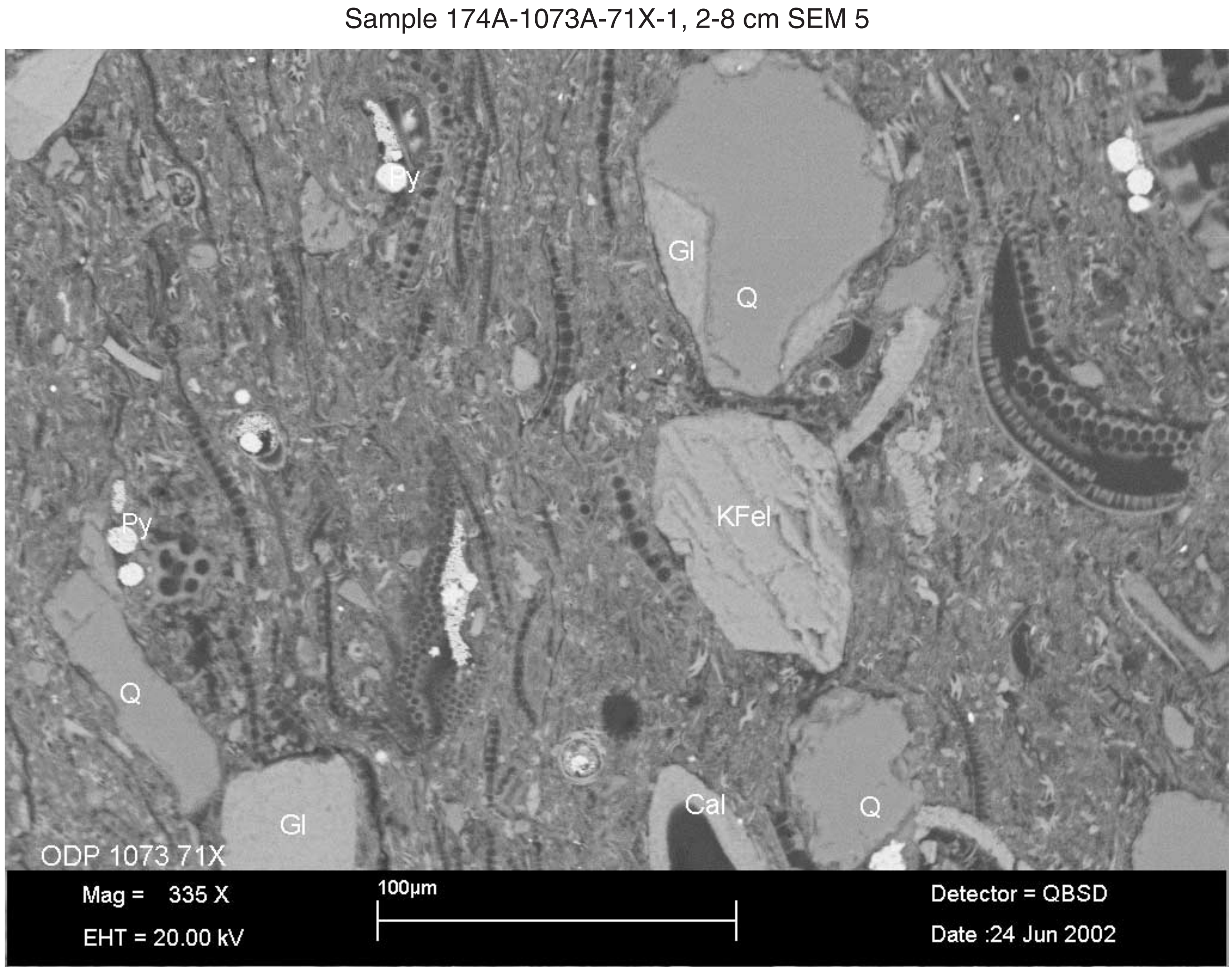

Figure AF31. SEM image at 1000×.

Sample 174A-1073A-71X-1, 2-8 cm SEM 6

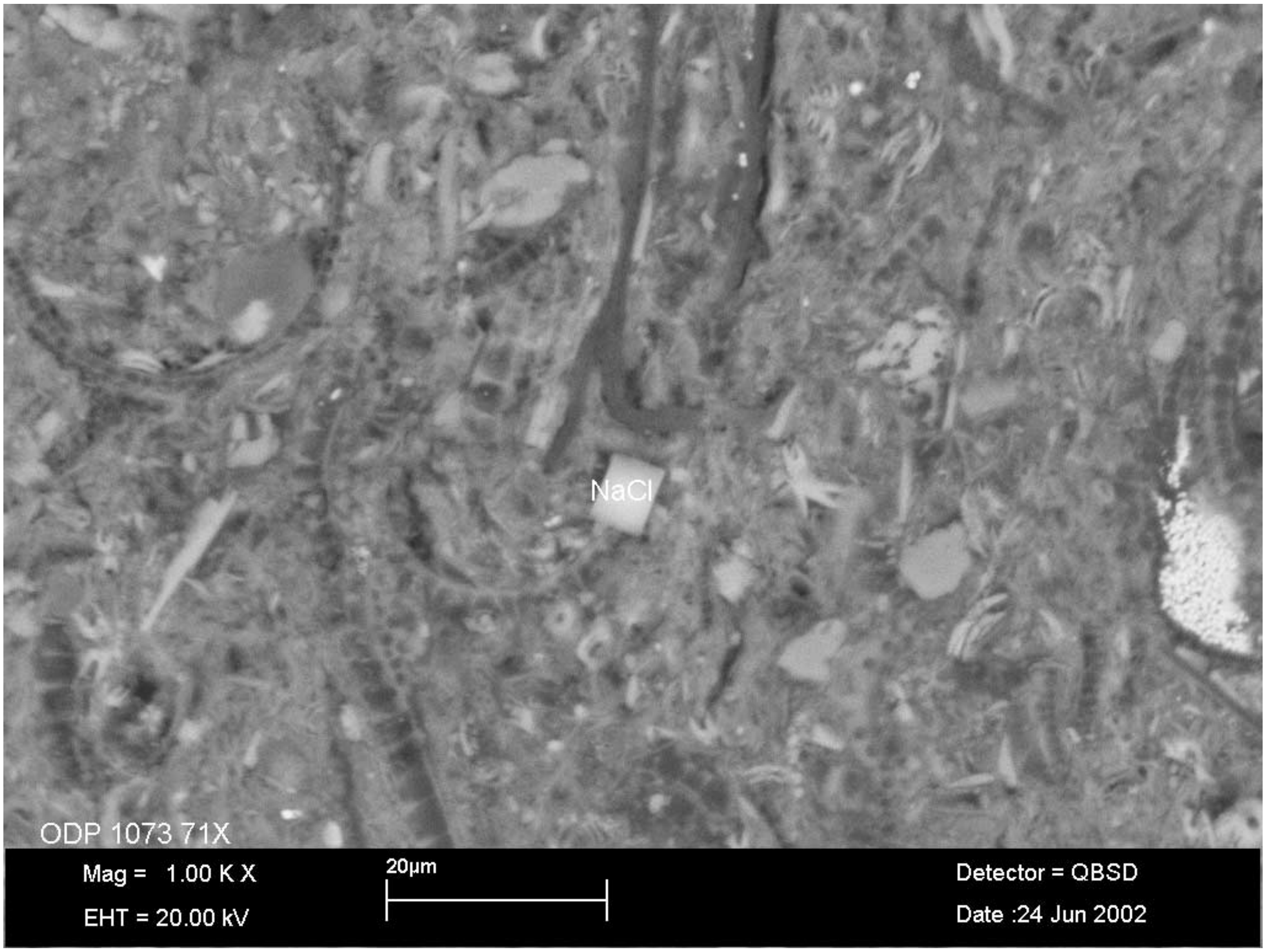

Figure AF32. SEM image at 1000×.

Sample 174A-1073A-71X-1, 2-8 cm SEM 7

Figure AF33. SEM image at 1000×.

Sample 174A-1073A-71X-1, 2-8 cm SEM 8